To the Graduate Council:

I am submitting herewith a thesis written by Roderick Greg Wamsley entitled "An Investigation of the V-I Characteristics of Electrical Discharges in Argon and Their Dependence on Gap Length and Pressure." I have examined the final copy of this thesis for form and content and recommend that it be accepted in partial fulfillment of the requirements for the degree of Master of Science, with a major in Physics.

Horace W. Crater

Dr. Horace W. Crater, Major Professor

We have read this thesis
and recommend its acceptance:

AAMason

Lloyd M Davis.

Brad Winkleman

John Lineberry

Accepted for the Council:

Cewminkel

Associate Vice Chancellor
and Dean of The Graduate School

STATEMENT OF PERMISSION TO USE

In presenting this thesis in partial fulfillment of the requirements for a Master's degree at The University of Tennessee, Knoxville, I agree that the Library shall make it available to borrowers under rules of the Library. Brief quotations from this thesis are allowable without special permission, provided that accurate acknowledgment of the source is made.

Permission for extensive quotation from or reproduction of this thesis may be granted by my major professor, or in his absence, by the Head of Interlibrary Services when, in the opinion of either, the proposed use of the material is for scholarly purposed. Any copying or use of the material in this thesis for financial gain shall not be allowed without my written permission.

Signature ______________________

Date 12-20-98

AN INVESTIGATION OF THE V-I CHARACTERISTICS OF ELECTRICAL DISCHARGES IN ARGON AND THEIR DEPENDENCE ON GAP LENGTH AND PRESSURE

A Thesis

Presented for the

Master of Science

Degree

The University of Tennessee, Knoxville

Roderick Greg Wamsley

May 1994

ACKNOWLEDGMENTS

First of all, I would like to express my thanks and appreciation to my work supervisors, Dr. Thomas Giel and Dr. Bradley Winkleman, for all of the confidence and cooperation that they gave to me during this project. Thanks also go to Prof. John Lineberry for his direction and helpful suggestions and to Dr. Horace Crater, for serving as my Major Professor. The other members of my thesis committee, Dr. A. A. Mason and Dr. Lloyd Davis also deserve and have my thanks and recognition for their help. I thank the United States Department of Energy and The University of Tennessee Space Institute for providing the environment and the financial support that made the attainment of this degree possible. Finally, I would like to convey some of the enormous gratitude I feel to my wife Jodee, for her continuing patience, support, and understanding throughout all of my graduate studies, and especially during the preparation of this thesis.

ABSTRACT

An analysis of the voltage-current characteristics of an electrical plasma discharge in a static argon environment has been conducted. Eight specific cylindrical electrode point to plane geometries were studied representing variations in electrode material, point cone angle and tip radii. Relations were developed governing characteristics such as threshold and breakdown voltages, critical field strength and general shape of the voltage vs. current (V-I) curve, of each of the Townsend, coronal and arc phases of the discharge. These relations were fit to experimental data to obtain approximate values for the unknown constants and to determine their variation with gap spacing and pressure. Trends in the V-I characteristics with respect to changes in electrode geometry have also been identified.

TABLE OF CONTENTS

CHAPTER PAGE

I. INTRODUCTION AND PURPOSE 1

II. EXPERIMENTAL SETUP 7

Static Test Cell 8

Electric Circuit 10

Data Acquisition System 14

Power Supply 16

Electrode Designs 17

III. THEORETICAL ANALYSIS 20

Background 20

Townsend Discharge 21

Corona Discharge 26

Arc Discharge 27

IV. EXPERIMENTAL RESULTS AND DISCUSSION 38

Threshold Voltage 40

Critical Field Strength 47

Breakdown Voltage 52

Shape of the Coronal V-I Curve 59

Shape of the Arc V-I Curve 65

V. SUMMARY AND RECOMMENDATIONS 78

Summary 78

Recommendations 81

LIST OF REFERENCES 82

VITA 85

LIST OF TABLES

TABLE PAGE

2.1. Control Variables and their Range of Values 7

2.2. Calibration of Isolation Amplifiers 15

4.1. Values for the Empirical Constants k_i in Equation 4.5 57

4.2. Values for the Empirical Constants k_i in Equation 4.8 66

4.3. Values for the Empirical Constants m_i in Equation 4.10 66

4.4. Values for the Empirical Constants k_i in Equation 4.14 76

LIST OF FIGURES

FIGURES PAGE

1.1. Simple illustration of the dynamics present in an MHD flow channel 2

2.1. Static test cell 9

2.2. Electric circuit schematic....11

2.3. Initial electrode set....18

2.4. Final electrode set: steel pins with very sharp points and copper pins with fixed cone angle and varying tip radii 19

3.1. Simplification of the arc column geometry....29

4.1. Sample of the simultaneous V-I curves obtained....39

4.2. Threshold voltage vs. onset current for the steel pins....41

4.3. Curve fits to threshold voltages for the steel pins 42

4.4. Threshold voltage vs. onset current for the copper pins 43

4.5. Curve fits to threshold voltages for the copper pins 46

4.6. Critical field strengths vs. *hp* for each of the eight pins 48

4.7. Curve fits of critical field strength to Equ. 4.2 for all eight pins 51

4.8. Breakdown voltage vs. *hp* for all eight pins....53

4.9. Slope and intercept of curve fits to V_b vs. *hp* 56

4.10. Breakdown voltage for the sharp copper pin with predicted curves from Equation 4.5 58

4.11. The parameters c_1 and c_2 from fit of coronas to Equation 4.6 for the 1.5 mm copper pin....60

4.12. The parameters k_0, k_1 and β resulting from curve fits of c_1 to Equation 4.7 for the 1.5 mm copper pin....61

4.13. Values of β resulting from fit with k_0 and k_1 held constant....63

4.14. The parameters η_1 and η_2 resulting from curve fits of c_2 to Equation 4.9 for the 1.5 mm copper pin....64

4.15. Parameters c_1 and c_2 with predicted curves from Equations 4.8 and 4.10 respectively, for the 1.5 mm copper pin....67

4.16. Variation of the average values for n of Equation 4.11 for the steel and copper pins....68

4.17. Parameter c_3 of Equation 4.11 resulting from curve fits of the arc region for all eight pins....70

4.18. Values of the fit constants η_3 and η_4 of Equation 4.12 as functions of pressure for the 1.5 mm copper pin....73

4.19. Values of the fit constants η_3 and η_4 of Equation 4.12 as functions of n for the 1.5 mm copper pin....75

4.20. Parameters c_3 with approximate curves from Equation 4.14 for the 1.5 mm copper pin....77

CHAPTER I

INTRODUCTION AND PURPOSE

The concept of generating electricity by flowing a conductive fluid through a region crossed by magnetic field lines, known as Magnetohydrodynamics (MHD), has been investigated for many years in the hope that it will become a major method of commercial and task-specific energy production. Traditional MHD power generation employs the heating of a working fluid or gas to create a thermally ionized plasma and passing that fluid through a channel in which there exists a magnetic field transverse to the flow. This flow of conducting gas then interacts with the magnetic field and induces an electric field $\vec{E}$ according to Faraday's law of induction,

$$\vec{E} = \vec{V} \times \vec{B}, \tag{1.1}$$

where $\vec{V}$ is the velocity of the working fluid and $\vec{B}$ is the applied magnetic field. This electric field, which is perpendicular to both the velocity of the fluid and the direction of the applied magnetic field, induces a current density, $\vec{J}$, in this same direction. Figure 1.1 shows an illustration of a simple MHD channel and the directions of the various dynamical quantities involved in this process.

Notice in Figure 1.1 the presence of a force, $\vec{F}$, opposite to the direction of the gas velocity. This force is termed the "*MHD braking force,*" a retarding force that arises from the fact that a current density in the presence of a magnetic field gives rise to a Lorentz force, $\vec{F}$, given by

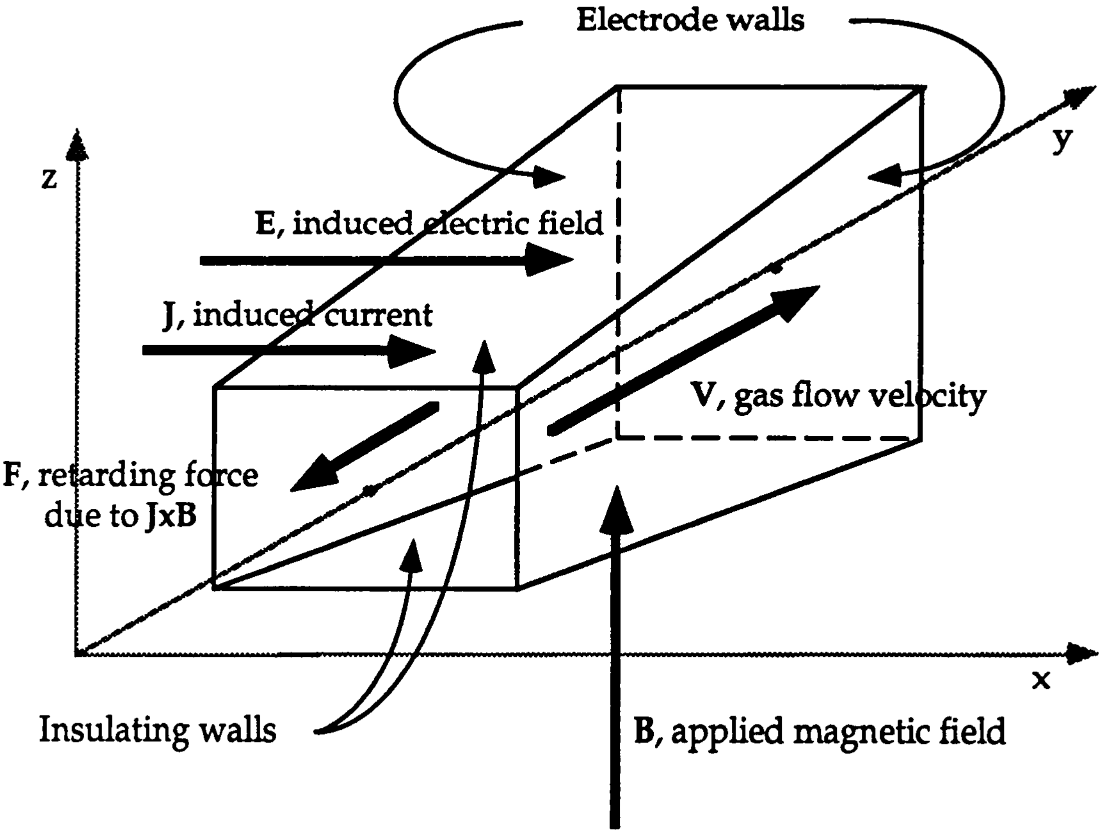

Figure 1.1. Simple illustration of the dynamics present in an MHD flow channel.

$$\vec{F} = \vec{J} \times \vec{B}. \tag{1.2}$$

In order for the gas to attain high velocities against this retarding electrodynamic force, a pressure gradient normally exists in the flow stream so that the gas can expand, pushing forward down the flow channel.[1]

Electric power is extracted from the system by tapping across the induced electric field to drive current through an external load. As shown in Figure 1.1, this is done by placing electrodes along the channel walls whose normals are parallel to the induced electric field and current density. Electrical energy removed from the system in this manner can then be stored and used for whatever purpose the generator was constructed for.

Because of the dependence of gas conductivity on temperature, the MHD power generation process requires heating the gas to very high temperatures, on the order of 2000 to 3000 K, in order to attain high enough conductivitys to make the process efficient. If the working fluid is not readily susceptible to thermal ionization, a chemically active seed element, such as cesium or potassium, can be added to the flow stream to further increase the conductivity of the fluid. This addition, however, can lead to costly seed recovery systems, and since a chemically active seed is very reactive and corrosive by nature, this can also lead to a significant reduction in the operational lifetime of the materials exposed to the fluid.

A different type of MHD generator has been proposed that utilizes a phenomenon known as the T-layer effect to attain the required conductivity necessary for efficient operation.[2] The T-layer effect arises from a local temperature perturbation somewhere in the flow which expands into the surrounding gas, creating a narrowly localized zone of increased temperature and conductivity. This localized zone of high temperature and conductivity is known as the T-layer. Since the working fluid is otherwise cold and non-conducting, it is not subject to the retarding Lorentz force and so tends to help push the T-layer down the flow stream. This "pushing" represents work done on the T-layer. Part of the resulting energy is released in the external load circuit as electrical energy, while part is thermal energy (Joule heat) expended to maintain the T-layer, resulting in a self-sustaining effect.

An MHD generator using the T-layer effect has notable advantages over the more traditional approach in that due to the high temperature of a developed T-layer (~10,000 K), the fluid's thermal ionization insures the existence of a high conductivity. This can preclude the need for costly seed additives and expensive seed recovery systems. Also, since the energy input to produce ionization is confined to the T-layer, the initial temperature of the working fluid need not be as high, allowing the selection of temperature at the MHD input to be determined by the thermodynamic cycle efficiency and extension of the channel service life.[2] The lower working temperature also has the added benefit of allowing conventional fluid flows to be used, e.g. air, rather than combustion products.

The local temperature perturbation that makes up the narrow conducting zone in a T-layer type generator can take the form of either an equilibrium or non-equilibrium plasma. In an equilibrium plasma the electron temperature is equal to the gas temperature, whereas in a non-equilibrium plasma the electron temperature can be orders of magnitude higher than that of the gas, resulting in greatly enhanced conductivity. With the proper choice for the working fluid, non-equilibrium effects can be enforced in a T-layer generator.

One way of creating a perturbation of this form is to use a plasma generation section at the beginning of the MHD channel in which an electrical plasma discharge is generated by application of a large potential across two electrodes exposed to the flow. The electrically ionized plasma created in this manner would subsequently move down the flow stream where its interaction with the magnetic field would produce the required self-sustaining T-layer.

This thesis arose as the starting point along a line of research whose end product would be the production of an optimized, electrical plasma discharge usable in initiating T-layers for this type of MHD power generator. There are many important factors that must be studied in pursuit of such a goal. Some of the more important ones are the characteristics of the discharge in gaseous environments. Characteristics such as voltage-current, (V-I), relationships, power requirements, and spatial distribution, as well as their dependencies on gap size, electrode geometry, and flow conditions must be looked at.

Therefore, a study was undertaken that looked at the dependencies of the V-I characteristics and spatial distribution on the factors mentioned above in the simplified environment of no flow. The purpose of this particular work was to provide a quantitative study of the dependence of coronal and arc voltage-current characteristics on electrode geometry, gas pressure, and gap spacing. This research was intended to accompany other work being done to characterize the spatial extent of the discharge, indicated by a discharge diameter, D, and its dependence on these same parameters as well as the overall power input. Taken together, these two studies represent a first step toward the goal mentioned above of producing a usable electrical plasma discharge for a T-layer type, MHD generator.

Chapter 2 focuses on the experimental procedure and setup for this study, detailing the type of data that was acquired as well as describing the equipment used to gather that data. The nature of the electrical discharge will be explained in Chapter 3, and elementary relations between different aspects of the V-I characteristics for the three phases of the discharge will be presented. Chapter 4 describes the results of the experiments and discusses the trends observed in the data in light of the relations given in Chapter 3, while a short summary of findings and some comments on the usefulness of this work as well as recommendations for future work are to be found in Chapter 5.

CHAPTER II

EXPERIMENTAL SETUP

The experimental work for this investigation involved the application of an electric potential across two metal electrodes separated by some variable distance in a static, pressurized, argon environment. The applied potential was then steadily increased until its maximum value was reached or until electrical breakdown occurred. Meanwhile, measurements of the voltage and current across the arc gap were carried out by a computer based data acquisition system.

The controlled variables for these tests and their ranges of possible values are given in Table 2.1. Each of these parameters were individually varied while the voltage vs. current curves were obtained at each step, in effect, filling a three dimensional array in which electrode, pressure, and gap

Table 2.1. Control Variables and their Range of Values.

Control Variable	Range
Gas Pressure	Atmosphere to Atm. + 50 psi in 10 psi steps
Arc Gap Spacing	0.05 to 1.0 inches in 0.05 in. steps
Electrode Design	Copper points, 30 degree cone angle: tip radii of <0.05 mm, 0.25 mm, 0.5 mm, 1.0 mm, and 1.5 mm Steel points, tip radii <0.05 mm: cone angles of 10°, 20°, and 30°

spacing were the indices and a V-I curve was the element.

Static Test Cell

The environment for the arc discharges consisted of a sealed, static test cell enclosing two vertically separated metal electrodes. In order to allow viewing of the discharge, the wall of the test cell was constructed from a section of a transparent, cylindrical, Plexiglas tube 11.4 cm high and 14 cm in diameter. Two square pieces of Micarta board, whose edges were 16.5 cm long, served as the top and bottom of the test cell. The general features of this test cell are illustrated in Figure 2.1.

The upper electrode was a flat copper plate 64 mm thick and 7 cm in diameter mounted to a vertical height adjusting mechanism and connected to an external electrical contact. The lower electrode was mounted on a fixed copper base plate and pedestal, also connected to an external electrical contact. Control of the gap spacing was administered by the vertical height adjusting mechanism, which was made of a half inch threaded rod connected to the upper plate electrode on one end and a 15.2 cm diameter Plexiglas wheel on the other. One full rotation of the wheel corresponded to an increase/decrease in height of 0.05 inches, or 1.27 mm, for the upper plate electrode, thus leading to a convenient measurement of gap spacing given in numbers of turns of the wheel, which were then converted to appropriate units.

The test cell was also equipped with a plastic supply hose, through which gas could be delivered to the cell, and an exit valve that allowed the cell to be vented at will. The gas used was delivered via pressure regulator from a 2000 psi bottle of commercially produced argon. The cell had the

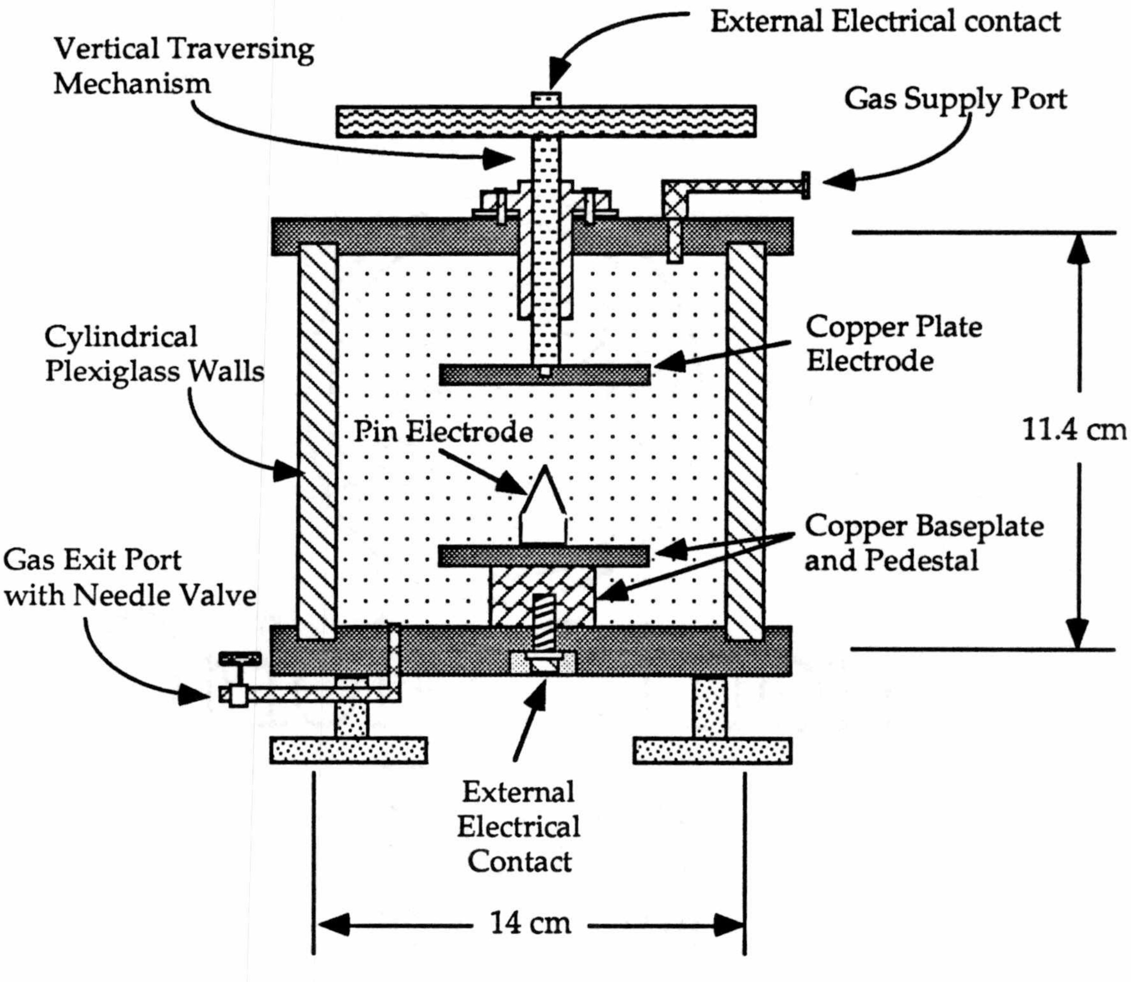

Figure 2.1. Static test cell.

capability of sustaining internal pressures of at least six atmospheres.

Electric Circuit

Because of the high powers involved in arc generation, it was necessary to create an electric circuit that would generate voltages low enough to be read by the computerized data acquisition system and that could be related to the quantities under study, namely the voltage and current across the gap. This was done by placing a voltage divider circuit in parallel with the gap while also placing current shunt resistors in series with the gap. Figure 2.2 is an illustration of the resulting circuit schematic showing the applied voltage, directions of current, voltage dividing resistors, arc gap, and current shunt resistors, as well as circuit protection devices (isolation amplifiers) and computerized data acquisiton system.

From Kirchoff's law it is known that the change in voltage around a closed loop must be zero, a fact that when applied to the circuit in Figure 2.2 immediately results in a relation among the voltages. Proceeding clockwise around the right hand loop yields

$$\Delta V = 0 = V_G + V_1 + V_2 - V_0 - i_2 R_1. \tag{2.1}$$

But from Ohm's law

$$i_2 = \frac{V_0}{R_0}, \tag{2.2}$$

giving

$$V_G = \left(1 + \frac{R_1}{R_0}\right) V_0 - (V_1 + V_2). \tag{2.3}$$

So, from the known values of R_1 and R_0 along with the measurements of V_0,

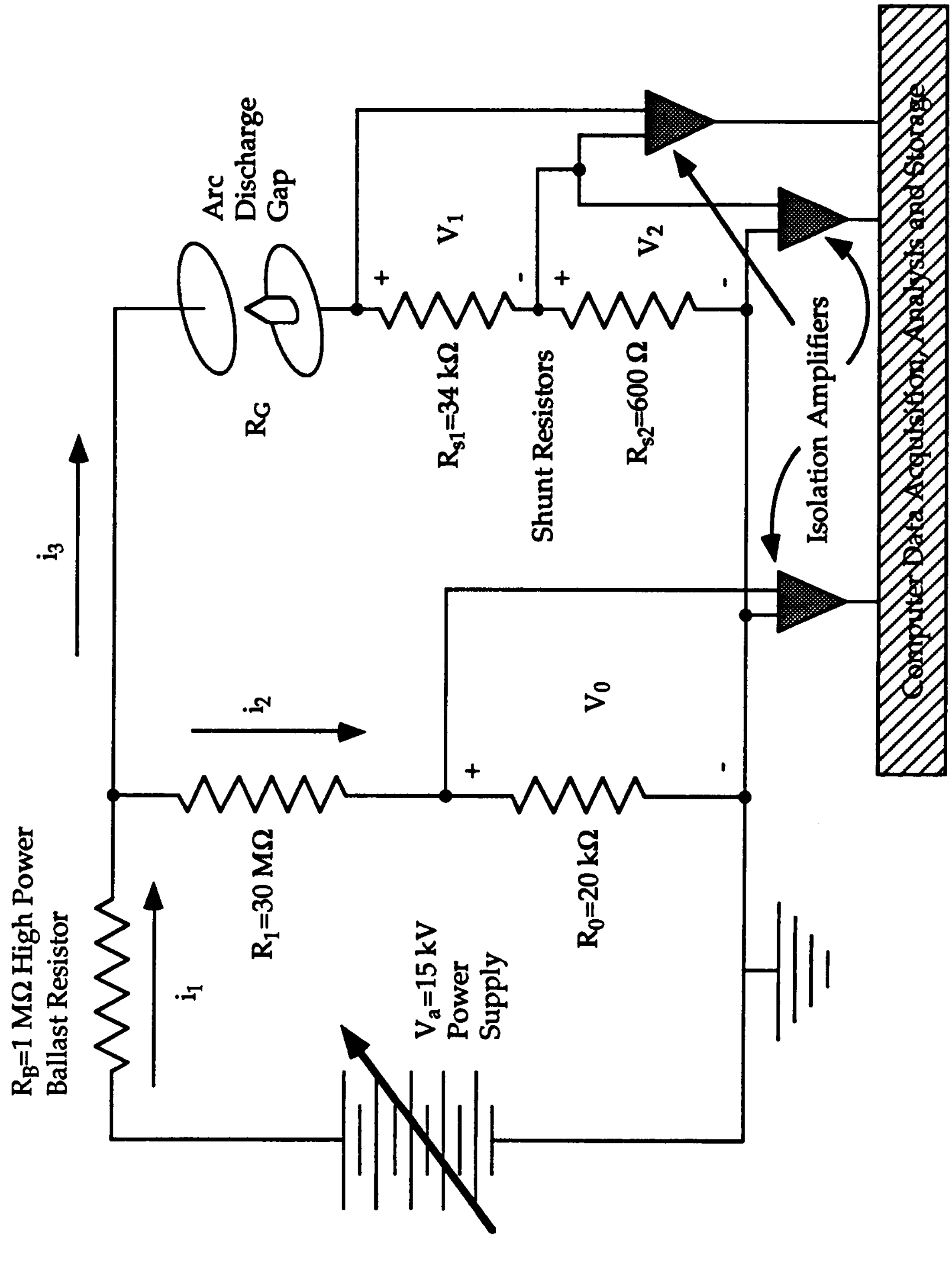

Figure 2.2. Electric circuit schematic.

V_1 and V_2, a value for the voltage across the gap, V_G, can be calculated using Equation 2.3. A value for the current crossing the gap, i_G, comes trivially from Ohm's law, as shown in Equation 2.4.

$$i_G = i_3 = \frac{V_1}{R_{S_1}} = \frac{V_2}{R_{S_2}}. \tag{2.4}$$

The current which passes through the gap can vary from nanoAmperes (nA) to Amperes (A), a variation of nine orders of magnitude, making it very difficult to accurately measure fluctuations in the lower current regimes without saturating the isolation amplifiers in the higher current regimes. A straightforward way of dealing with this problem was to have two current shunts, R_{S1} and R_{S2}, where R_{S1} was sized to cover currents up to ~ 3×10^{-4} A and R_{S2} was chosen to produce signals appropriate for currents on the order of 10^{-4} A to 15 mA.

The resistor values used during these tests were as follows: $R_B = 1.00$ MΩ, $R_0 = 20.03$ kΩ, $R_1 = 29.55$ MΩ, $R_{S1} = 34.62$ kΩ, $R_{S2} = 602.8$ Ω. The ballast resistor, R_B, consisted of a group of five high power ceramic resistors connected in series. Each of these ceramic resistors was approximately 200 kΩ and capable of dissipating about 60 to 80 Watts. In this study the resistor bank served only to prevent a power supply overload by limiting the current passing through the gap under breakdown conditions. However, this is not the only role that the ballast resistor plays in the arc generation process. The arc gap possesses a capacitance, which together with the ballast resistor determines a time constant for the transition to full arc. In this way the value of the ballast resistor plays an important role in the initiation of breakdown and the stability of the arc.

With the values given above for R_B, R_{S1}, and R_{S2}, the maximum current through the gap can be seen to be no more than 14.5 mA under breakdown conditions, given a maximum applied voltage of 15 kV. This current would produce a maximum potential drop across R_{S1} of 502 V and of 8.74 V across R_{S2}. Protection for the computerized data acquisition system from the still high voltages across R_{S1} and any other stray voltages or breakdowns that might occur elsewhere in the circuit was attained by two separate measures.

The first precaution taken was the placement of GE-MOV® varistors in parallel with each of the 3 resistors across which voltage was being measured. These devices act as open switches for operating voltages less than their 30 volt threshold, but for any voltage above that value they will allow current to pass, thereby preventing the buildup across these low power resistors of any excessive voltages that might occur due to transient surges in the circuit.

Secondly, the gap circuit and the computerized data acquisiton system were separated by high voltage wide band isolation amplifiers. The isolation amplifiers passed input voltages of less than their 10 V threshold but output only 10 V for any input greater than that value, effectively limiting the voltages going into the data acquisition system to no more than 10 V, the limit of the system. In addition, the very high input impedances of the amplifiers, at least $10^{12}\ \Omega$, were much higher than the values of the resistors in the gap circuit and thereby isolated the amplifiers from the rest of the circuit, insuring accurate voltage measurements.

Although these isolation amplifiers exhibited exceptional linearity in their operating range of 0 to 10 V, they showed gains of approximately 0.9. The amplifiers were calibrated to allow for this non-unity gain error as well as to correct any nonlinearities that might be present. This was done by applying a known voltage source to the amplifiers' inputs and measuring the output across the 10 V range. The input voltage, known accurately to four significant digits, was increased from 0 to 10 V in 0.05 V steps while the output was measured at each step by the computer. The measured values were then plotted against the known values and fit to a linear curve. A measure of the linearity of the response was obtained from values of the mean squared deviation calculated during the fit. The mean squared deviation is simply an average of the squared difference between the actual data and the linear fit at all points along the line. An upper limit for this mean squared deviation was found to be approximately $4x10^{-5}$. Table 2.2 shows the slopes and y-intercept values obtained from several different calibration runs for each of the three isolation amplifiers, along with their mean and standard deviations.

Data Acquisition System

As indicated above, data from these tests were collected by a computer based data acquisition system, the main component of which was an Apple Macintosh Quadra 950 computer. The setup of this system required the creation of several objects known as Virtual Instruments (VIs) with a software application package called LabVIEW®, developed by National Instruments Corporation. Rather than purchasing hardware instrumentation to perform desired functions, the user can create, using LabVIEW®'s graphical programming method, instruments that will perform those same functions but reside on the computer's hard drive along with the operating LabVIEW® software. When a LabVIEW® instrument is opened, the user is presented with the instrument's Front Panel, where all of the instrument controls and

Table 2.2. Calibration of Isolation Amplifiers.

Run #	V_0 Channel		V_1 Channel		V_2 Channel	
	Slope	Intercept	Slope	Intercept	Slope	Intercept
1	.91263	.24526	.91056	.23487	.90944	.09562
2	.91262	.24542	.91045	.23586	.90933	.09560
3	.91260	.24537	.91057	.23498	.90934	.09662
4	.91243	.24578	.91056	.23489	.90955	.09528
5	.91251	.24550	.91044	.23576	.90952	.09558
Mean	.91256	.24547	.91052	.23527	.90944	.09574
St. Deviation x 10^{-5}	7.7	18	5.9	44	8.9	46

indicators are located. All operations involved in the operation of the instrument are directly controlled from the Front Panel of the VI.

Analog voltage levels from the isolation amplifiers were fed into the analog input channels of a National Instruments' NB-MIO-16H data acquisition board, where they were converted to digital signals and read by a VI created by the author specifically for these tests. During operation, the VI scanned the three input channels at a frequency of 50 kHz, giving a 20 μs time lag between each channel read. Since only the overall features of the voltage-current curve during the coronal and arc phases of discharge were of interest in this study, and not the time resolved nature of the transitions, this 20 μs lag was considered negligible, and these measurements were assumed to be simultaneous. The three channels as a group were scanned at a rate determined by the execution time of the VI's programming, a rate that was measured to be approximately 40 Hz.

The voltages obtained in the manner described above were then adjusted by the VI to compensate for the response of the isolation amplifiers using the values for slope and intercept obtained during calibration, and subsequently converted to values for V_G and i_G using Equations 2.3 and 2.4, followed by the display of the values on a Front Panel strip chart as they were acquired. The arrays of values were then displayed in graphical form and stored to disk when the VI's execution was stopped.

Power Supply

The high voltage necessary for the generation of the arc discharges was supplied by a regulated, high voltage, D.C. power supply, a Universal Voltronics Corp. model #BRE 15-60A-S. This supply was manually adjustable from 0 to 15 kV and limited to about 70 mA of current, much more than the 15 mA needed to sustain an arc at the maximum applied voltage in this circuit configuration.

Electrode Designs

Two sets of electrodes were used in this study. Initially, the performances of five general electrode types, shown together in Figure 2.3, were evaluated in order to focus later testing on specific geometrical variations of the most promising ones, as determined by low power consumption and large spatial distribution.

The first electrode of this initial set was a very sharply pointed steel pin constructed by hand on a metal lathe out of a 5/16" threaded bolt. The second electrode used was also a steel pin, commercially available with a straight shaft and a smooth rounded tip. The third was a conical copper pin also hand tooled on a lathe from a 5/16" threaded copper bolt. Lastly, two other smaller copper pins cut from 3/16" copper bolts were used, one with a straight shaft and rounded tip, the other with conical shaft and rounded tip.

Figure 2.4 shows the final set of electrodes, which consisted of three steel pins and five copper ones. The three steel electrodes were each conical pins with very sharp points, representing a variation in cone angle, the first at 10°, second at 20°, and third at 30°. The five copper pins represented a variation in tip radius of curvature with a fixed cone angle of 30°, increasing from a very sharp tip to 0.25 mm, 0.5 mm, 1.0 mm, and 1.5 mm radii. When viewed under a microscope, the four sharp electrodes were all observed to have tip diameters of less than 0.05 mm.

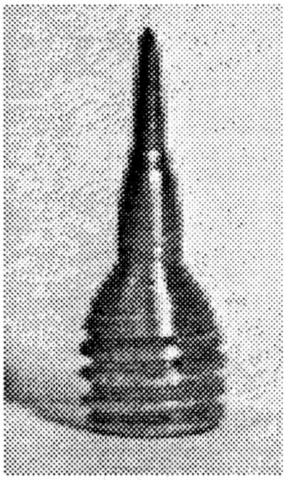

Steel Pin

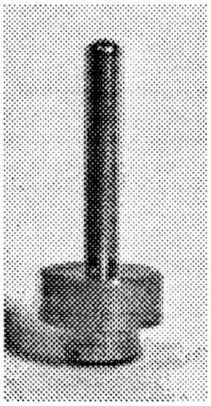

Commercial Steel Pin

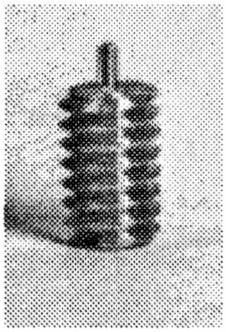

Small Sraight Copper Pin

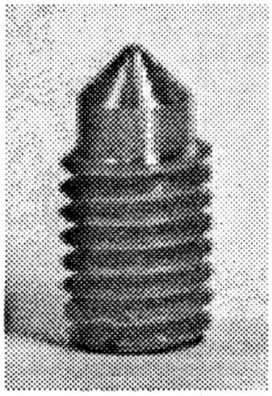

Large Copper Conical Pin

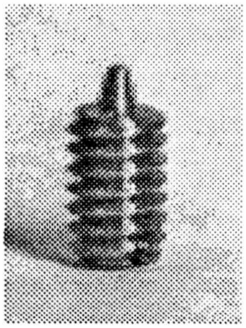

Small Conical Copper pin

Figure 2.3. Initial electrode set.

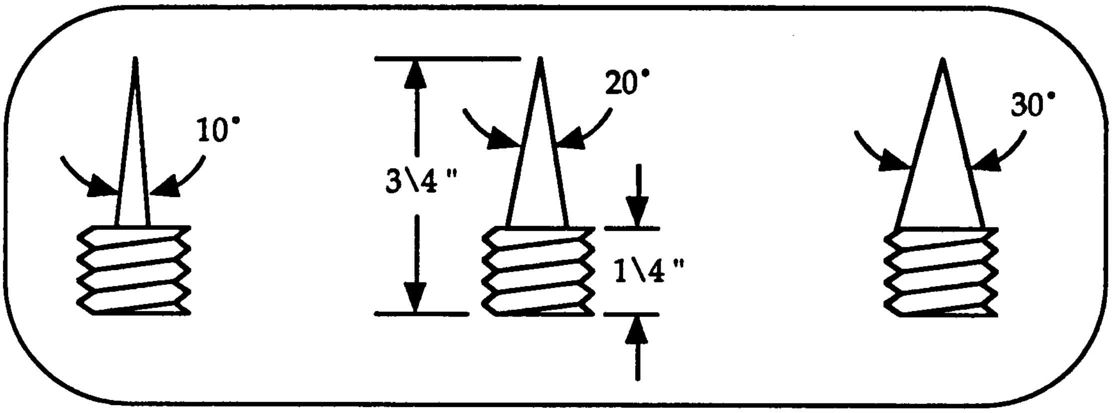

(a)

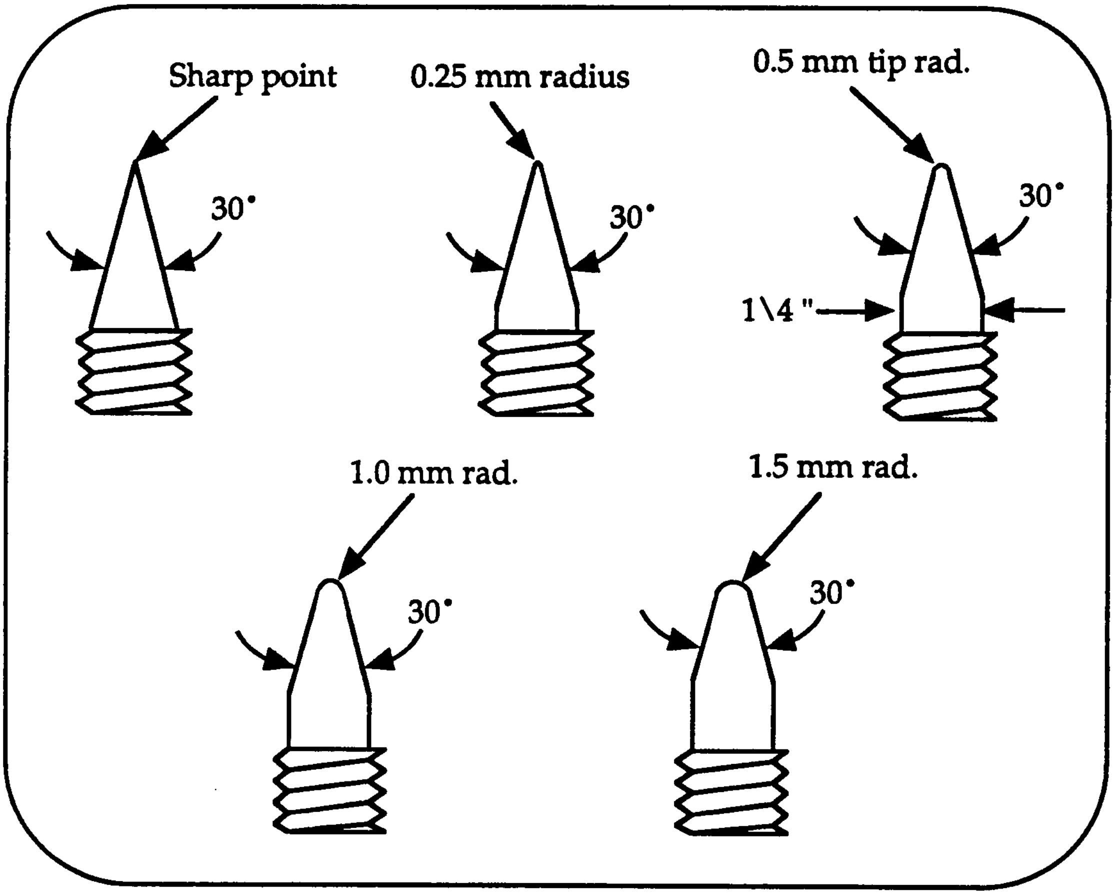

(b)

Figure 2.4. Final electrode set: steel pins with very sharp points (a) and copper pins with fixed cone angle and varying tip radii (b).

CHAPTER III

THEORETICAL ANALYSIS

Background

The breakdown of a gas into an electrical plasma discharge progresses through several phases and over a current range of up to nine or ten orders of magnitude. This chapter will first present a brief description of an electrical plasma discharge and the different phases in which it manifests itself. Later, some relations for each phase of the discharge describing the dependence of arc size and V-I characteristics on the parameters of electrode geometry, gas pressure, gap spacing, and power input will be derived

The word *discharge* means "the equalization of a difference of electric potential between two points by a transfer of electricity."[3] This definition would imply that once the potential was equalized the discharge would cease, indicating a transient phenomenon. In fact, it is the constant attempt to equalize the potential that makes most discharges steady state phenomena.

Gaseous discharges are broken into two main categories,[4] those which are self-sustaining and those which are not. Non self-sustaining discharges, usually called *dark* or *Townsend* discharges, are characterized by the fact that the current ceases with the removal of the external ionizing source, such as background radiation. Self-sustaining discharges, on the other hand, result from the ionizing effect of the voltage gradient being applied and require no external ionizing source. These are called *glow, corona* or *arc* discharges.

Transitions between a Townsend and corona discharge are characterized by either a sharp jump in current or the appearance of a luminous glow or halo around the electrode with the larger electric field, or possibly both. The transition between the corona phase and the arc phase is known as *breakdown* and is accompanied by a sharp drop in voltage, sharp increase in current, and the formation of a luminous column bridging the two electrodes in which there is complete, or nearly complete, ionization of the gas, resulting in very high conductivity.

It must be understood that the values of the threshold and breakdown voltages and the exact shape of the V-I curve in each of the three regions are very much dependent on the gas type, gas pressure, electrode type, and discharge gap length. Again, characterizing and quantifying these quantities for electrode configurations useful for T-layer MHD generators is the purpose of this study.

Townsend Discharge

In a Townsend discharge it is usually assumed that there exists a finite, but very small, number of free electrons and ions present in the gas volume of interest, due perhaps to photoionization or some other source of background radiation. Upon the application of an electric field to this volume, these electrons will be accelerated toward the positively charged anode, while the positive ions will be accelerated toward the negatively charged cathode.

The accelerated electrons will move in straight lines under a uniform field until they collide with neutral particles. If an electron has gained sufficient energy (on the order of the ionization energy of the gas atom) due to this acceleration, then this collision will most likely remove an electron from the outer shell of the neutral atom, ionizing the atom and introducing into the system another electron-ion pair. Since it will have lost most of its energy in the collision, the original electron, along with the newly created one, will again gain energy by being accelerated by the electric field, and the process repeats itself, resulting in an avalanche effect as these electrons progress toward the anode. The same effect occurs as the ions progress toward the cathode, but because of their much greater mass, the ions move very slowly resulting in considerably fewer ion-neutral collisions.

The electron-neutral ionization process can be described by the parameter α, Townsend's first ionization coefficient, defined as the number of ionizations per electron per unit length. With $n_e(x)$ defined as the number density of electrons in a given volume (both those already present and those created by ionization),

$$dn_e = \alpha\, n_e(x)\, dx \tag{3.1}$$

represents the total number of additional electrons produced along a length dx by electron-neutral ionization. So

$$\frac{dn_e}{dx} = \alpha\, n_e(x), \tag{3.2}$$

which is easily integrated giving

$$n_e(x) = n_e(0)\, e^{\alpha x}, \tag{3.3}$$

where $n_e(0)$ is the initial electron number density at the cathode.

There also exists a secondary process that contributes to the release of electrons, the process of electron emission by impact ionization. Some ions reaching the cathode will have sufficient energy (on the order of the work function for the electrode material) to eject electrons upon impact with the surface. This process is described by γ, Townsend's second ionization coefficient, defined as the number of electrons released by impact for every ion striking the cathode. Now, the total electron current density at the cathode, j_{ec}, is due to both the initial, j_{e0}, and secondary, j_{es}, cathode current densities,

$$j_{ec} = j_{e0} + j_{es}. \tag{3.4}$$

The total current density at the cathode, j_c, is a combination of j_{ec} and the ion current density, labeled j_{ic},

$$j_c = j_{ec} + j_{ic} = j_{e0} + j_{es} + j_{ic} \quad . \tag{3.5}$$

But $j_{es} = \gamma j_{ic}$ from the definition of γ, so

$$j_c = j_{ec} + \frac{j_{es}}{\gamma} = j_{e0} + \left(1 + \frac{1}{\gamma}\right) j_{es}. \tag{3.6}$$

Note that the total current density at the anode, j_a, is approximately given by $j_a \approx j_{ea}$, since there is no significant secondary emission of ions, and conservation of current at the anode and cathode requires that $j_a = j_c$. Substituting this relation into the first form of Equation 3.6 and eliminating j_{es} gives

$$j_{ec} = \frac{j_{e0} + \gamma j_{ea}}{1 + \gamma}. \tag{3.7}$$

The next step follows from recognizing that j_{ea}, the total electron current density at the anode is larger by a factor $exp(\alpha h)$ than the total electron current density at the cathode according to Equation 3.3. Therefore,

$$j_{ea} = j_{ec}\, e^{\alpha h}. \tag{3.8}$$

Using Equation 3.8 to eliminate j_{ec}, the resulting equation for the total current density, $j = j_{ea}$, is

$$j = \frac{j_{e0}\, e^{\alpha h}}{1 - \gamma\left(e^{\alpha h} - 1\right)}. \tag{3.9}$$

A condition for the breakdown into a self-sustaining discharge is obtained by observing when the denominator of Equation 3.9 vanishes. If we neglect 1 relative to $e^{\alpha h}$ ($\gamma << 1$), then the breakdown condition is

$$\gamma e^{\alpha h} = 1. \tag{3.10}$$

The energy that an electron gains by being accelerated by an electric field will depend on the strength of that field and the distance the electron travels between collisions, the mean free path L. For a very large mean free path the electron travels a large distance between collisions resulting in fewer encounters, and for small L the number of collisions necessarily goes up, so that the number of new electrons produced in a unit length of path by the accelerated electron will be inversely proportional to L. This relationship between L and the electron producing collisions suggests an equation for α of the form

$$\alpha = \frac{f(EL)}{L}, \tag{3.11}$$

where $f(EL)$ denotes some function of the product of L and an idealized, uniform electric field defined by $V = Eh$. Since the mean free path, L, is inversely proportional to the gas pressure, p, ($1/L = Ap$, where A is some constant), α can be expressed as

$$\frac{\alpha}{p} = g\left(\frac{E}{p}\right), \tag{3.12}$$

where g is some function to be determined. For estimation purposes a functional form for α can be found to be,[5]

$$\alpha = A\, p\, e^{-\left(\frac{B\, p}{E}\right)}, \tag{3.13}$$

where the constant A is that same proportionality constant relating p and the mean free path, L. The exponential dependence in Equation 3.13 comes from the fact that the number of free paths greater than a given distance is a decreasing exponential function of the distance. If the probability of causing ionization for those electrons with energy greater than the ionization energy is assumed to be unity, then the number of new electrons produced will depend on how many electrons travel far enough to gain this much energy, giving a form for α as shown in Equation 3.13. This indicates that the constant B is related to the effective ionization energy of the gas.

Equation 3.13 allows an approximate value for the breakdown voltage, V_b, to be calculated from the breakdown condition, Equation 3.10.

$$ln\left(\frac{1}{\gamma}\right) = A\, h\, p\, e^{-\left(\frac{B\, h\, p}{V_b}\right)}, \tag{3.14}$$

or

$$\frac{A\, h\, p}{ln\,(1/\gamma)} = e^{\left(\frac{B\, h\, p}{V_b}\right)}, \tag{3.15}$$

and taking the natural logarithm of both sides yields

$$V_b = \frac{B\, h\, p}{ln\left[\frac{A\, h\, p}{ln\,(1/\gamma)}\right]}. \tag{3.16}$$

Corona Discharge

The corona discharge is typically a self-sustained discharge that has not reached complete breakdown, and exhibits a luminous *crown* or brush-like formation around the electrode with the smaller radius of curvature, and therefore, higher electric field. The threshold voltage for the formation of the corona, as well as the type of corona itself, is dependent on whether the stressed electrode (larger electric field) has a positive potential relative to the other electrode (positive corona), or a negative potential relative to the other electrode (negative corona). All of the tests done here were carried out with a negative corona.

Early this century, Townsend conducted extensive studies[6] of the voltage-current characteristics of coronas in a cylindrical geometry (a wire or small cylinder surrounded by a larger, coaxial cylinder) and derived a relation giving the current per unit length of the conductor as a function of the applied voltage, between the two cylinders of radii r and R ($r < R$), and the threshold voltage V_S:

$$i_G = \frac{2\,\mu\, V_G\,(V_G - V_S)}{R^2\, ln\,(R/r)}, \qquad (V_G \geq V_S) \tag{3.17}$$

where the mobility, μ, is assumed to be independent of the electric field, E.

Although Equation 3.17 is specific to cylindrical geometries, a relation of similar form has been shown to apply to other configurations as well, such as the point to plane geometry.[7] That relation is

$$i_G = C\, V_G\,(V_G - V_S), \tag{3.18}$$

where C is an empirical constant dependent on gap spacing and pressure.

Arc Discharge

The arc discharge, as indicated earlier, generally occurs as an optically bright discharge column with currents on the order of 0.1 Amperes or higher. This plasma column typically has very high conductivity resulting from the high degree of ionization of the gas. The voltage-current traces of an arc discharge are marked by a breakdown voltage, V_b, the voltage at which the transition from Townsend or corona discharge to full arc takes place, and by the fact that the voltage generally increases as the current decreases. These factors, as with the cases of Townsend and corona discharges, are also dependent upon the type of electrodes, gas type, gas pressure, and gap spacing.

When dealing with arc discharges another factor also becomes important, the spatial extent of the actual column, characterized by the arc diameter, D. Investigations into the size of the arc and its dependence on power input are necessary to determine how much of the gas volume is actually ionized in or around an arc and whether or not this can be expanded. In a T-layer ionizing section, it would be beneficial to successfully ionize the entire cross sectional area of the flow in order to get the maximum use of the T-layer. This means that larger arc diameters would reduce the number of arcs needed in the ionizer section while also increasing the performance of the generator.

The size of the arc column is directly dependent upon the power being fed into the arc. High power arcs have a fairly wide spatial distribution while low power dissipation results in small arc diameters. This can be seen by looking at the energy balance for a simplified arc column.

The first step is to approximate the arc column as a cylinder of gap height h and diameter D, as shown in Figure 3.1. When the arc is in thermal equilibrium, the internal heat generated will balance that being transferred across the boundary. Mathematically this gives an energy balance equation for a stabilized arc as,

$$Q \pi D h = q_i \pi \frac{D^2}{4} h, \tag{3.19}$$

where Q is the net heat flux across the boundary (Wt m^{-2}), and q_i is the rate of internal heat generated per unit volume (Wt m^{-3}). The internal heat generated arises from Joule heat dissipation, or

$$q_i = \vec{J} \cdot \vec{E} = \sigma E^2, \tag{3.20}$$

where the current density, $\vec{J}$, is given by Ohm's Law,

$$\vec{J} = \sigma \vec{E},$$

in terms of the electrical conductivity, σ (S m^{-1}), and the applied electric field, $\vec{E}$ (V m^{-1}). The average conductivity can be expressed in terms of the overall impedance of the arc, R_G, obtained from values of the gap voltage and values of the current through the gap measured during a discharge, as

$$\sigma = \frac{4h}{R_G \pi D^2}. \tag{3.21}$$

Combination of Equations 3.19, 3.20, and 3.21 yields an expression for the arc diameter:

$$D = \frac{E^2 h}{R_G \pi Q}. \tag{3.22}$$

The voltage across the gap, however, is approximated as $V_G = Eh$, and the current through the gap is $i_G = Eh/R_G$, so Equation 3.22 becomes

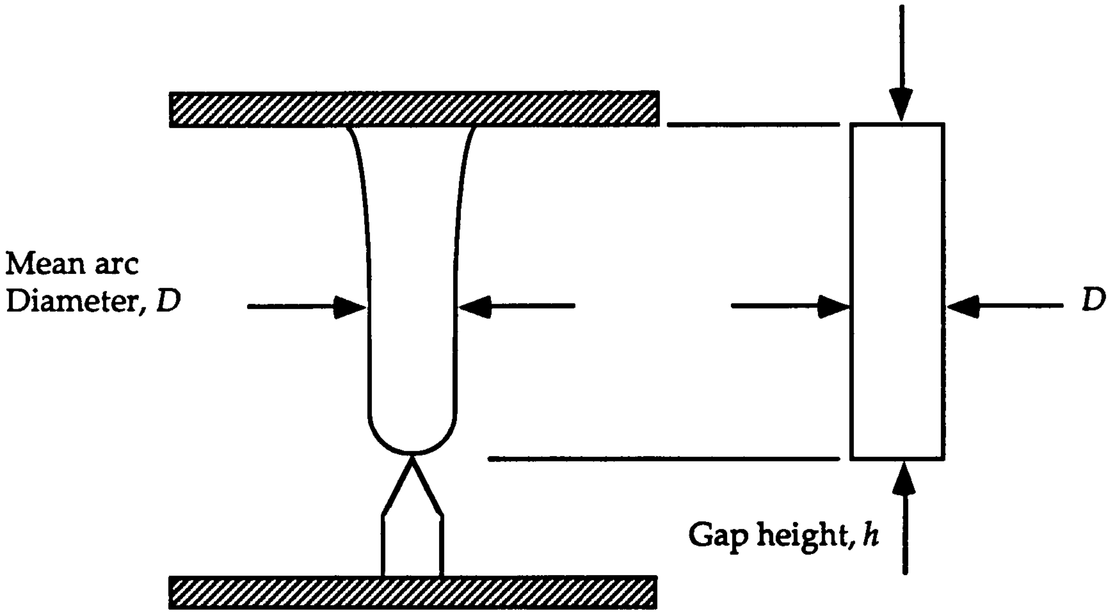

Figure 3.1. Simplification of the arc column geometry.

$$D = \frac{V_G\, i_G}{\pi\, h\, Q} = \frac{P}{\pi\, h\, Q}, \tag{3.23}$$

where P is the electrical power supplied to the arc.

From this relation it is apparent that the diameter of the arc is directly proportional to the power supplied to the arc while inversely proportional to the net heat flux across the wall of the arc, for fixed arc length. This would indicate that if the power to the arc increased faster than the heat flux across the boundary, then the arc diameter would increase, while if the heat flux increased faster than the power supplied to the arc, the diameter of the discharge would decrease.

The energy flux across the boundary of any arc will be due to a combination of three effects: radiation, conduction, and convection. It is usually assumed[8] that for very high temperature (~10,000 K and higher) and high pressure arcs, the heat transfer process is radiation dominated allowing the conduction and convection terms to be neglected in the energy balance analysis.

Using radiation transfer theory and a few simplifying assumptions it can be shown [9],[10] that the integrated radiation energy flux is given by

$$Q = F(\chi)\, \sigma_B\, T^4, \tag{3.24}$$

where $\sigma_B = 5.7\text{x}10^{-12}$ Wt cm^{-2} K^4 is the Stefan-Boltzmann constant and T is the absolute temperature of the plasma in Kelvins (K). $F(\chi)$ is a dimensionless coefficient dependent on the average extinction coefficient χ, over the radiation spectrum, and χ is defined as the inverse of the mean free path of photons in the material of interest, a coefficient describing the amount of energy lost by passage of radiation through that material. Therefore, it is evident from Equations 3.23 and 3.24 that in the very high temperature regime, the diameter of the arc is inversely proportional to the absolute temperature (to the fourth power).

On the other hand, for lower temperature, low current arcs the radiation process does not contribute significantly to the total energy transfer.[11] Therefore, in the analysis below, closely following that by Suits and Poritsky,[12] radiation has been neglected while conduction and convection are considered as the dominant terms in the energy transfer.

In this analysis, the arc column is considered as a hot cylindrical solid body, introducing some error due to the fact that convection currents for a solid body are zero at the surface, while for an arc column they are at a maximum there. The heat loss due to convection currents within the arc column are also neglected, since they are on the order of 7% of the total loss.[13]

By means of dimensional analysis, all of the parameters describing the heat transfer from hot cylinders can be simplified into three dimensionless groups dependent on one another. The resulting relation between these three groups of parameters is shown in Equation 3.25.

$$\left(\frac{hD}{\kappa}\right) = f\left[\left(\frac{D^3\beta_0\rho^2 g\,\Delta T}{\eta^2}\right)\left(\frac{c_p\eta}{\kappa}\right)\right] \tag{3.25}$$

Here, h is the coefficient of convective heat transfer (Wt m^{-2} K^{-1}), D is the diameter of the cylinder (m), κ is the thermal conductivity (Wt m^{-1} K^{-1}), ρ is the density (kg m^{-3}), β_0 is the coefficient of thermal expansion (K^{-1}), g is the acceleration due to gravity (m s^{-2}), η is the viscosity (kg s^{-1} m^{-1}), c_p is the specific heat at constant pressure (J kg^{-1} K^{-1}), and ΔT is the temperature difference between the body and the ambient fluid.

The three dimensionless constants shown in parentheses in Equation 3.25 are known as the *Nusselt*, *Grashof*, and *Prandtl* numbers respectively. The Nusselt number can be interpreted physically as the ratio of the temperature gradient in the fluid immediately in contact with the surface to the reference temperature gradient, $\Delta T/L$, where L is a characteristic length of the system. The Grashof number represents the ratio of buoyant to viscous forces in the heat transfer process, in general a function of the Reynolds number. But, when buoyancy is the only driving force, i.e. for free convection, the velocity of the fluid is determined entirely by quantities in the Grashof number, and the Reynolds number is superfluous. The Prandtl number can be looked at as the ratio of two molecular transport properties, the kinematical viscosity, which affects the velocity distribution, and the thermal diffusivity, which affects the temperature profile. In other words it relates the velocity distribution to the temperature distribution.

It can be shown[14] that for free convection, the Nusselt number, hD/κ, depends only on the product of the Grashof and Prandtl numbers. Furthermore, comparison with experimental data for tests in liquids and gasses over extremely large ranges for these three numbers, shows that f is an exponential relation of the form

$$\frac{hD}{\kappa} = const\left[\left(\frac{D^3\beta_0\rho^2 g\,\Delta T}{\eta^2}\right)\left(\frac{c_p\eta}{\kappa}\right)\right]^{\alpha}, \tag{3.26}$$

where α ranges from .04 to .25. The Prandtl number, $c_p\eta/\kappa$, is constant for gases, having the value .73 for diatomic gases and .67 for monatomic gases, and so can be absorbed into the constant. Also, in the approximation of a ideal gas, $\beta_0 = 1/T$ and $\rho = mp/RT$, where m is the molecular weight of the gas, p is the pressure (kg m^{-2}), T is the absolute temperature (K), and R is the gas constant (m K^{-1}). With these facts, Equation 3.26 becomes

$$\frac{hD}{\kappa} = const\left(\frac{D^3 m^2 p^2 g\ \Delta T}{T\eta^2 R^2 T^2}\right)^{\alpha}. \tag{3.27}$$

It is useful here to define a mean film temperature, T_f, as

$$T_f = T_{ambient} + \frac{\Delta T}{2}, \tag{3.28}$$

in order to avoid difficulties that arise from the fact that the temperature varies considerably within the film surrounding the arc, resulting in uncertainties in the dimensionless constants. Because of this, it is customary to evaluate the gas constants at T_f.

By replacing h with $\frac{W}{\pi D \Delta T}$, where W is the heat lost per unit length of arc (J m^{-1}), h becomes

$$h = \frac{Ei_G}{\pi D \Delta T}, \tag{3.29}$$

where E is the apparent potential gradient (V m^{-1}) and i_G is the current through the gap (A). Substitution into Equation 3.27 yields

$$Ei_G = \left(\kappa_f \Delta T\right) const\left(\frac{D^3 m^2 p^2 g\ \Delta T}{\eta^2 R^2 T^3}\right)^{\alpha}, \tag{3.30}$$

where κ_f is the value of κ at the mean film temperature.

Employing the simplifying assumption that for constant pressure the arc temperature has only a very small effect on the arc current and can therefore be neglected, the relations between E, i_G, and D can then be obtained simply as functions of the physical properties of the ambient gas, namely,

$$Ei_G = const\ D^{3\alpha}. \tag{3.31}$$

The arc current is expressed in terms of n_e, the electron concentration, and K_e, the electron mobility, as

$$i_G = \pi\left(\frac{D}{2}\right)^2 n_e e K_e E. \tag{3.32}$$

But, Saha's equation[15] says that for constant pressure, n_e is a function of temperature only, so

$$i_G = const\ D^2 E, \tag{3.33}$$

and eliminating D, Equations 3.31 and 3.33 give

$$Ei_G = const\left(\frac{i_G}{E}\right)^{\frac{3\alpha}{2}}, \tag{3.34}$$

or solving for E,

$$E = const\ i_G^{-n}, \tag{3.35}$$

where $n = \frac{2-3\alpha}{2+3\alpha}$. For the values of α given earlier, the exponent n will lie on the range $.45 < n < .89$. In Chapter 4, Equation 3.35 will be fit to experimental data to provide empirical values for the muliplicative constant and the exponential constant, n.

Above, it was noted that the Saha equation gave n_e as a function of T only for constant pressure, but if the pressure is allowed to vary and the dependence of arc temperature on gas pressure is taken into account, n_e as a function of pressure can be written as

$$n_e = const\ p^{\beta}, \tag{3.36}$$

where β is an empirical constant that must be determined from experimental data showing the variation of T with pressure.

If the effect of temperature on the electron's mean free path and average velocity is neglected, the electron mobility, K_e of Equation 3.32, will vary as $1/p$.[16] Using this, Equations 3.32 and 3.36 give

$$i_G = const\, D^2 p^{\beta-1} E. \tag{3.37}$$

Similarly, in the equation of heat transfer, Equation 3.30, the dependence of temperature on the right hand side, appearing mainly in the terms κ_f ($\sim T^{3/4}$) and ΔT ($\sim T$), can be neglected in comparison with the much larger effect of temperature variation in n_e. Now, from $W = Ei_G$,

$$\frac{dW}{W} = \frac{di_G}{i_G} + \frac{dE}{E}, \tag{3.38}$$

and by taking logarithmic differentials of Equation 3.37,

$$\frac{di_G}{i_G} = 2\frac{dD}{D} + \frac{dE}{E} + (\beta - 1)\frac{dp}{p}. \tag{3.39}$$

Also, for Equation 3.30,

$$\frac{dW}{W} = 3\alpha\frac{dD}{D} + 2\alpha\frac{dp}{p}. \tag{3.40}$$

First, note that if p is held constant, $dp = 0$, and using Equation 3.40 in Equation 3.38 yields

$$3\alpha\frac{dD}{D} = \frac{di_G}{i_G} + \frac{dE}{E}, \tag{3.41}$$

and eliminating dD/D between Equations 3.39 and 3.41 gives

$$\frac{dE}{E} + \frac{di_G}{i_G}\left(\frac{\frac{2}{3\alpha} - 1}{\frac{2}{3\alpha} + 1}\right) = 0. \tag{3.42}$$

The solution of which is

$$E = const\; i_G^{-\left(\frac{2-3\alpha}{2+3\alpha}\right)} = const\; i_G^{-n}. \tag{3.43}$$

Equations 3.43 and 3.35 are identical since their derivations were essentially the same, following only slightly different routes.

Now, if the current were considered as constant, $di_G = 0$, and a relation giving the arc diameter as a function of pressure can be obtained in a similar manner. Using Equation 3.38 in Equation 3.40 gives

$$3\alpha\frac{dD}{D} + 2\alpha\frac{dp}{p} - \frac{dE}{E} = 0. \tag{3.44}$$

Eliminating dE/E in Equations 3.39 and 3.44 results in

$$\frac{dD}{D} + \frac{dp}{p}\left(\frac{2\alpha + \beta - 1}{3\alpha + 2}\right) = 0, \tag{3.45}$$

giving a solution of the form

$$D = const\; p^{-\left(\frac{2\alpha+\beta-1}{3\alpha+2}\right)} = const\; p^{-\gamma}, \tag{3.46}$$

which expresses the dependence of the arc diameter, D, on the pressure, p, in terms of the exponent α, from the heat balance equation, and the experimental constant β, obtained from the variation of electron density with pressure and temperature.

Finally, if instead dD/D were eliminated from Equations 3.39 and 3.44, with i_G still held constant, the result would be

$$\frac{dE}{E}\left(\frac{1}{2} + \frac{1}{3\alpha}\right) + \frac{dp}{p}\left[\frac{(\beta - 1)}{2} - \frac{2}{3}\right] = 0, \tag{3.47}$$

and

$$E = const\ p^{-\frac{\alpha[3(\beta-1)-4]}{(3\alpha+2)}} = const\ p^{m}. \qquad (3.48)$$

Thus, based upon the assumptions 1) that radiation does not play a significant role in heat transfer across the arc boundary at low temperatures and low currents, 2) that the relationship between the physical factors in the heat balance equation is the same as for heat loss from a solid body, and 3) that the variation of temperature with current at constant pressure is small enough to be neglected, relations for the arcing phase of an electrical discharge have been obtained that express the apparent electric field, E, as a function of the current through the gap, i_G, for constant pressure,

$$E = const\ i_G^{-n}, \qquad (3.35)$$

also as a function of the pressure, p, for constant current,

$$E = const\ p^{m}, \qquad (3.48)$$

and that express the arc diameter, D, as a function of the pressure for constant current,

$$D = const\ p^{-\gamma}. \qquad (3.46)$$

CHAPTER IV

EXPERIMENTAL RESULTS AND DISCUSSION

As was mentioned at the beginning of Chapter 2, the data taken during these experiments consisted of two voltage-current traces for every combination of pin type, gas pressure, and gap spacing shown in Table 2.1, one covering the low current detail of the Townsend and corona regions and another showing the high current range of the arc discharge. A sample pair of these simultaneous traces is shown in Figure 4.1.

The traces in Figure 4.1 were traced out through the complete range of voltage, both increasing up through breakdown and decreasing down through arc extinction. Normally there will be some hysteresis present in V-I traces, as the values for threshold and breakdown voltages will be different depending on whether the voltage is increasing or decreasing. This phenomenon is especially apparent when observing the difference between the arc breakdown voltage, V_b, and the arc extinction voltage. Depending on the value of the ballast resistor, the extinction voltage may be drastically lower than V_b. Figure 4.1(a) illustrates the clearly visible transition from Townsend to corona discharge, marked by threshold voltage V_s, as well as the arc extinction voltage occurring for decreasing voltage. Figure 4.1(b) shows the full current range of the arc region, while in both figures the transition from corona to arc, marked by breakdown voltage V_b, is clearly visible.

Most of the analysis in the following sections involved the use of a commercial application package called IGOR® to display and manipulate the

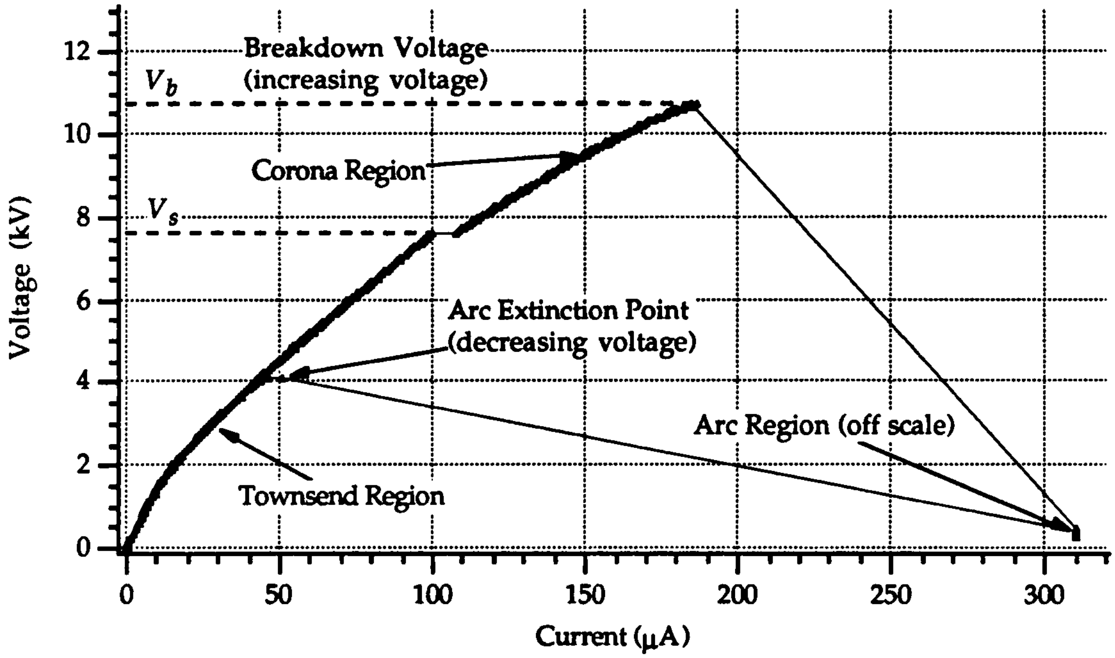

(a)

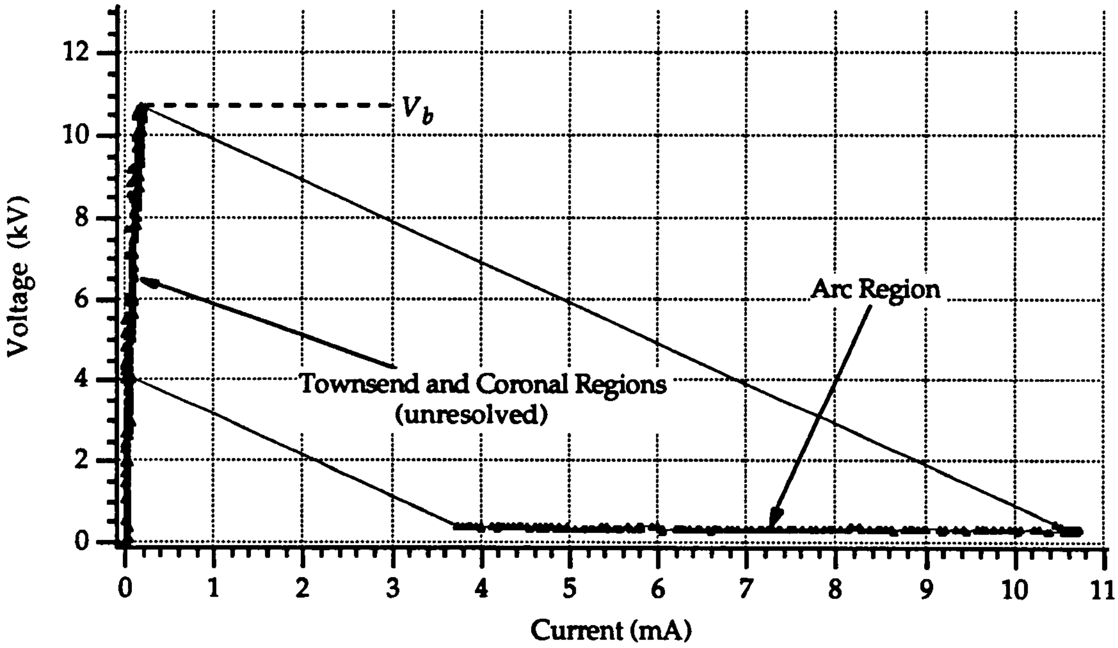

(b)

Figure 4.1. Sample of the simultaneous V-I curves obtained.

data from these V-I traces. Since a good portion of the analysis required some curve fitting with IGOR®, an explanation of the method used is in order. IGOR® uses iterative curve fitting operations to find fit coefficients which minimize a multi-dimensional error function. It uses the Levenberg-Marquardt algorithm, a non-linear least squares routine, to search the multi-dimensional error space. IGOR® sees the error function as a surface in the error space and iteratively chooses fit coefficients that take it to a valley on this surface. There may be other deeper valleys on the surface, however, but intelligent initial guesses for the coefficients will increase the chances that IGOR® will find the deepest valley, thus representing the best fit.

Threshold voltage

The first obvious task was to plot the point of corona onset as given by V_s and i_s and see how it varied with pressure for each of the pin types. Figure 4.2 shows this type of plot for the three steel pins. It is evident from this figure that as the pin cone angle was increased, the corona onset point became more stable and experienced less variation with changes in gas pressure. Also shown in the figure are the most likely threshold currents for any given voltage, represented by a curve fit of the form $V_s = a_1 i_s^{b1}$. Graphs of the curve fits for the three steel pins are shown together in Figure 4.3. Notice that for any given threshold voltage, V_s, the corona onset current decreases with increasing cone angle. As the pin becomes more needle-like, the onset current increases on average but becomes more unstable, and V_s is affected to a larger extent by the pressure.

Each of the copper pins had a cone angle of 30 degrees and varied from one another in their point radii. In Figure 4.4, the threshold voltages and

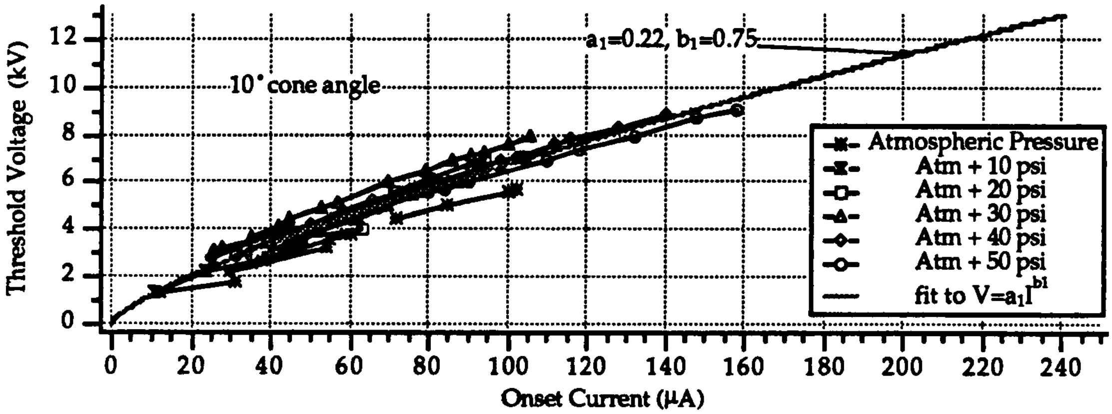

(a)

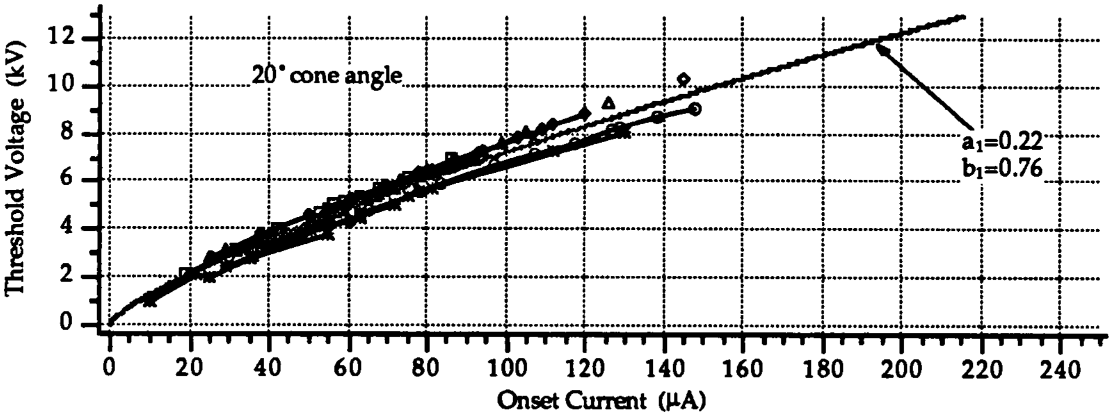

(b)

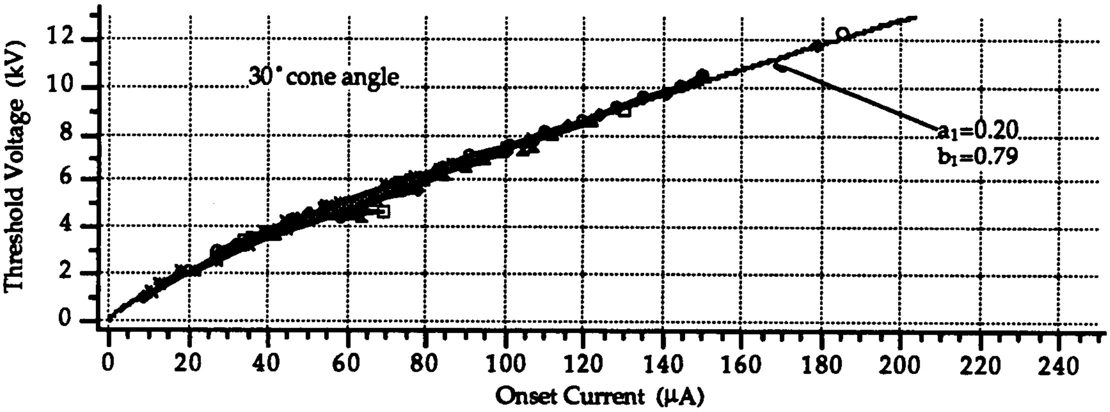

(c)

Figure 4.2. Threshold voltage vs. onset current for the steel pins.

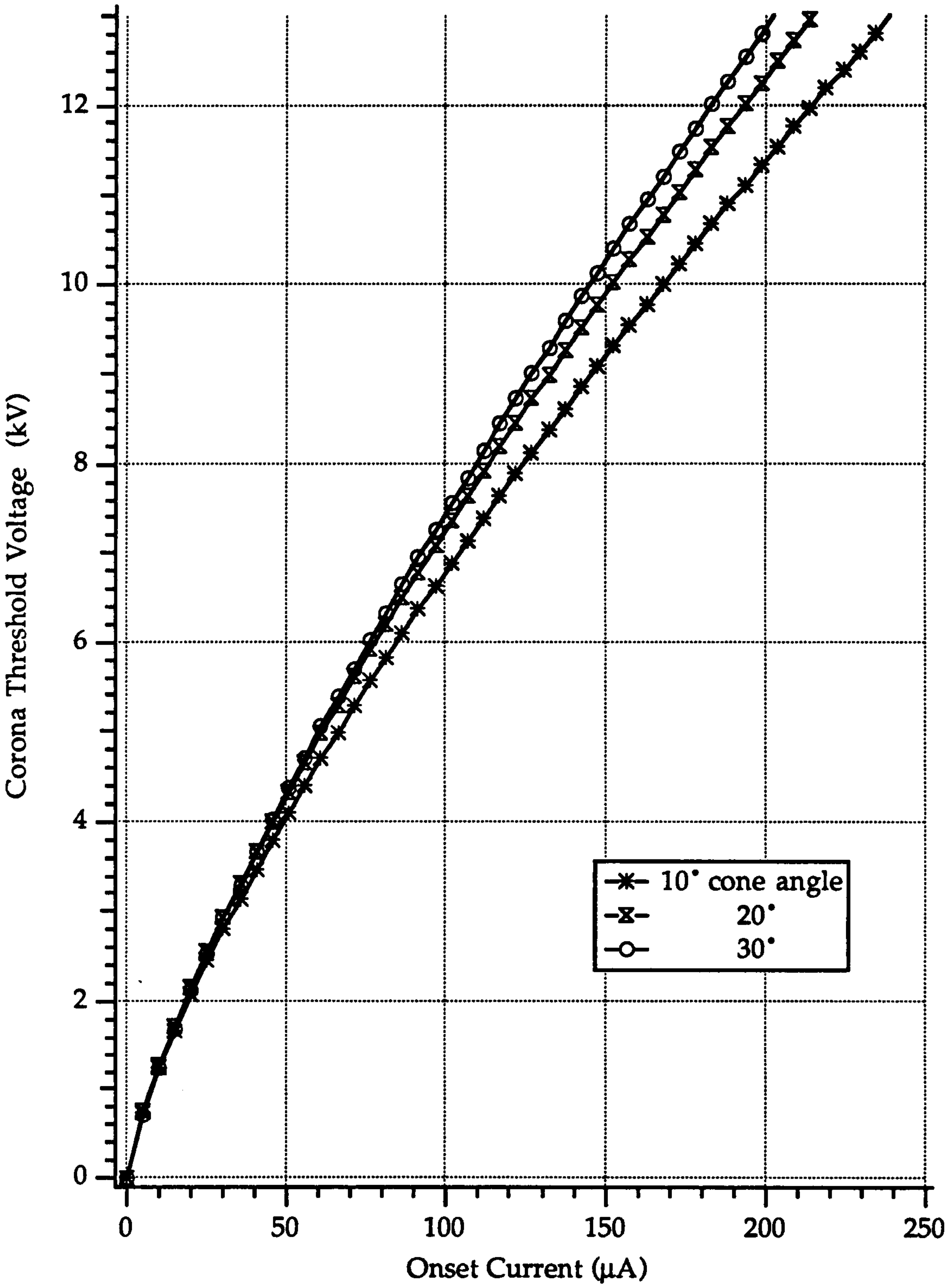

Figure 4.3. Curve fits to threshold voltages for the steel pins.

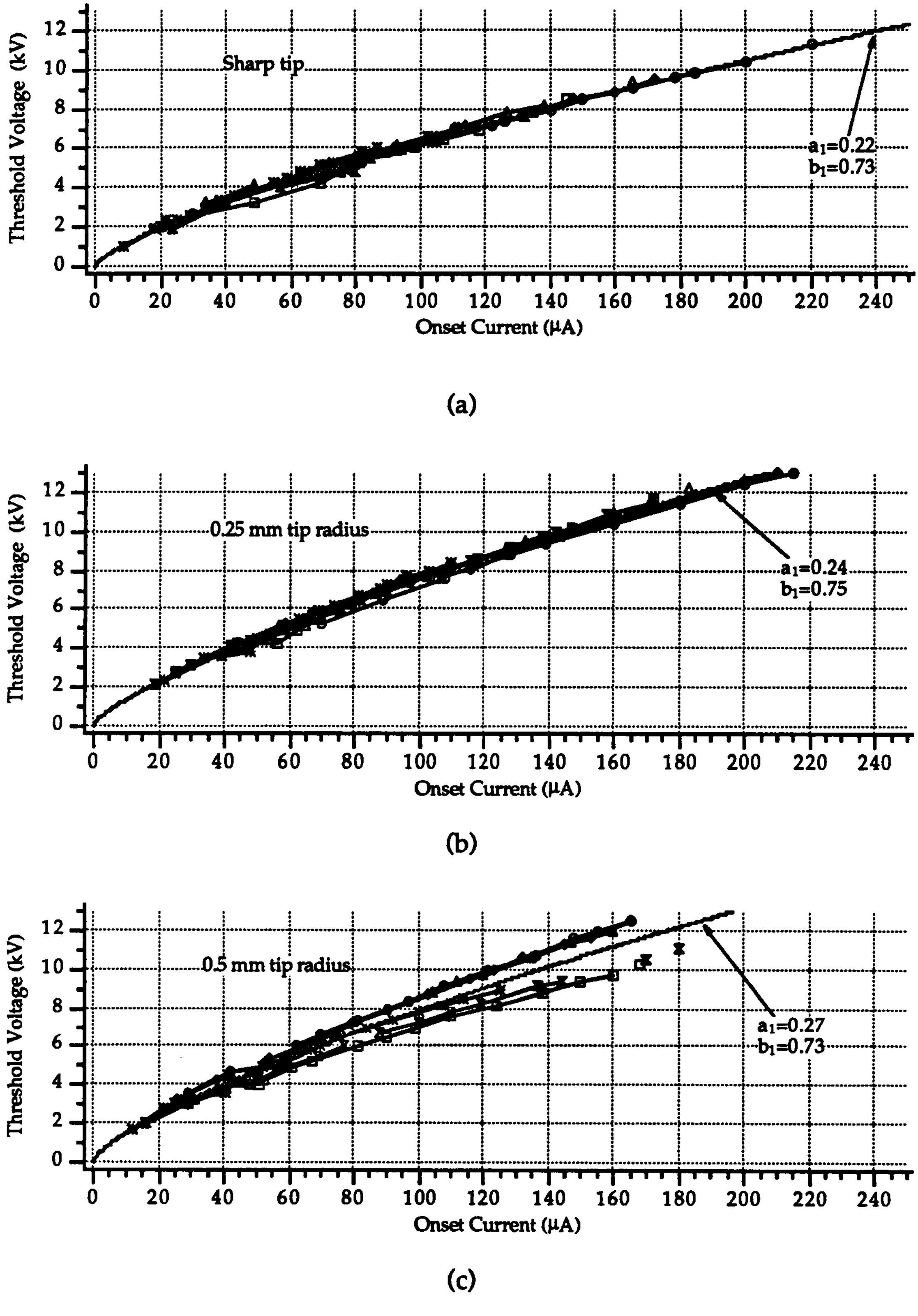

Figure 4.4. Threshold voltage vs. onset current for the copper pins.

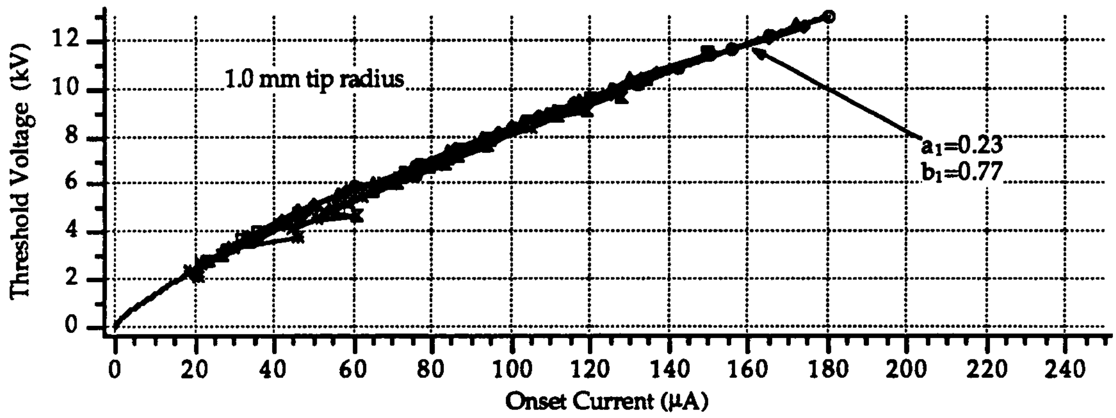

(d)

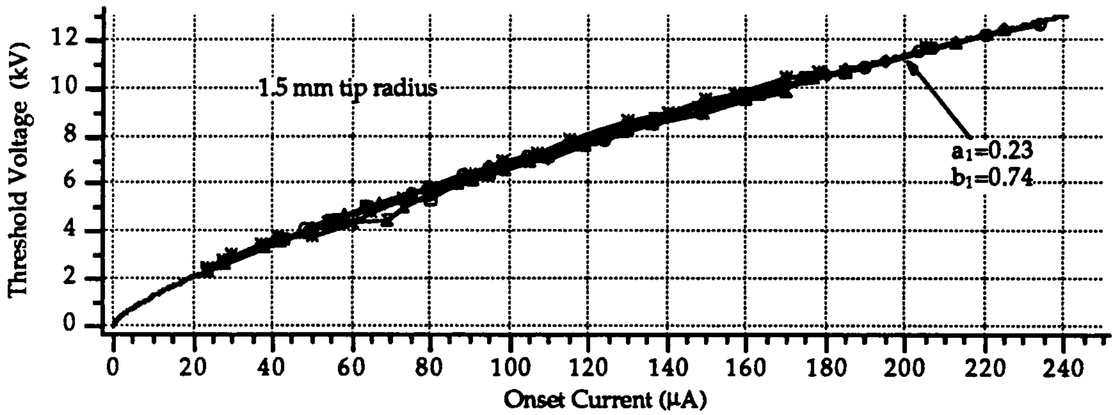

(e)

Figure 4.4 (continued)

curve fits are plotted against the threshold current for the five copper pins. The only one showing a significant variation with pressure is the 0.5 mm radius copper pin. The curve fits for these five pins, shown together in Figure 4.5, also exhibit an increase in onset current for a given threshold voltage as the pin becomes more needle-like. As the point radius decreases, the onset current increases in every case except for the transition from the 1.5 mm point to the 1.0 mm point.

One possible explanation for these deviations, is that there may have been inhomogeneities in the pin structure that would have affected the electric field in the neighborhood of the point, thereby altering the threshold characteristics. The condition of the electrode surface is a very important factor in the characteristic response of that electrode. Alterations of the surface condition, such as contamination by foreign materials, oxidation or corrosion of the metal, or changes in polishing techniques can have dramatic effects on the values of threshold or breakdown voltages.

To alleviate these difficulties, an attempt was made to be as consistent as possible in the preparation of both the electrode pins and the upper plate electrode. Before each of the pins was installed in the static test box, that pin and the upper plate electrode were first smoothed with a piece of fine grit sand paper and then polished with the paper backing of that same piece of sand paper. This procedure had the effect of removing any metal ridges that may have formed during manufacture of the electrodes, and of removing the bulk of any oxidation that may have formed on the electode from its exposure to air, as well as smoothing out the scratches left by the abrasive sandpaper.

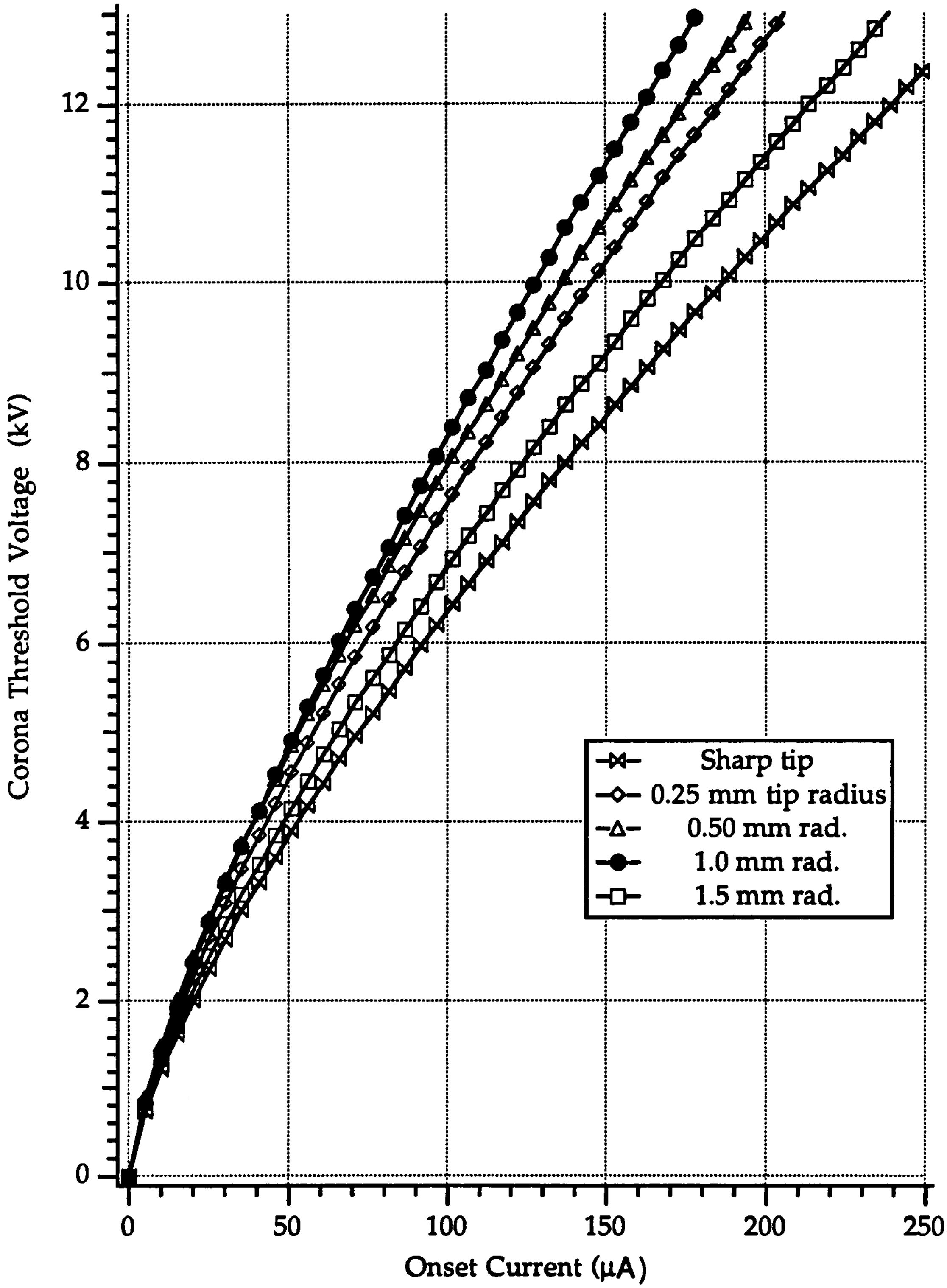

Figure 4.5. Curve fits to threshold voltages for the copper pins.

Critical Field Strength

In Chapter 3 it was found that an approximate value of the breakdown voltage could be calculated from Equation 3.16 if the constants A, B and γ are known. Because of the simplification of the processes involved under breakdown conditions, this relation actually applies more to the threshold voltage for formation of the corona than to the full arc breakdown voltage. With this in mind, Equation 3.16 is then of the form

$$V_s = \frac{a_2\,(hp)}{b_2 + ln(hp)}, \tag{4.1}$$

and is seen to be only a function of the product of the gap distance and the pressure. Dividing the equation by hp gives a relation for the *apparent* critical field strength

$$\frac{E_s}{p} = \frac{a_2}{b_2 + ln(hp)}. \tag{4.2}$$

E_s is labeled apparent because it is an approximate, uniform electric field given by $E_s = V_s/h$.

In order to test the validity of Equation 4.2, the values for the critical field strengths were determined from the experimental data and curve fit to this equation. Figure 4.6 shows the apparent critical field strengths plotted as the product of gap distance and pressure, hp, for each of the eight pins along with a curve fit to Equation 4.2. From these figures it is clear that the premise stated above about V_s being only a function of hp holds true, at least for the sharply pointed pins. But when the radius of curvature was 0.25 mm or above, lines of constant pressure began to emerge, as illustrated in Figure 4.6(f), being most apparent at low pressure (745 and 1262 mmHg). Figure 4.7 shows the curve fits to Equation 4.2 for each of the eight pins plotted together,

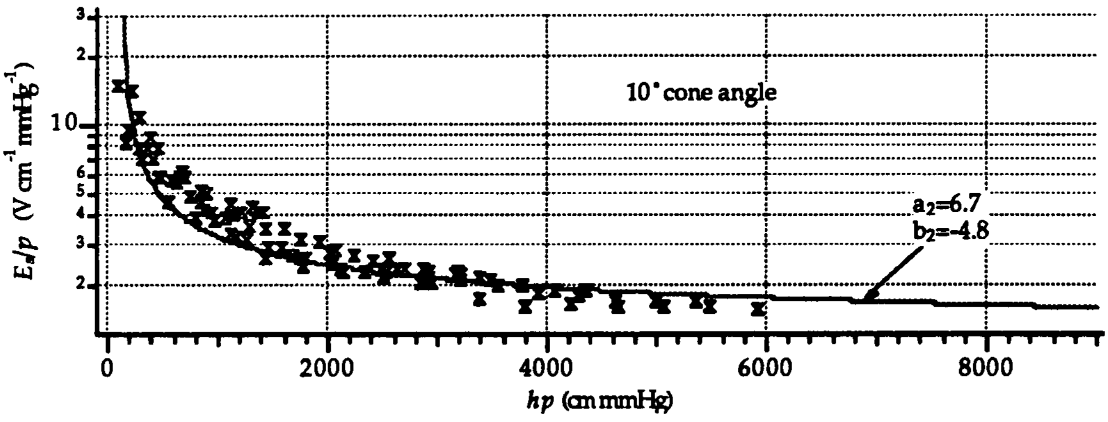

(a)

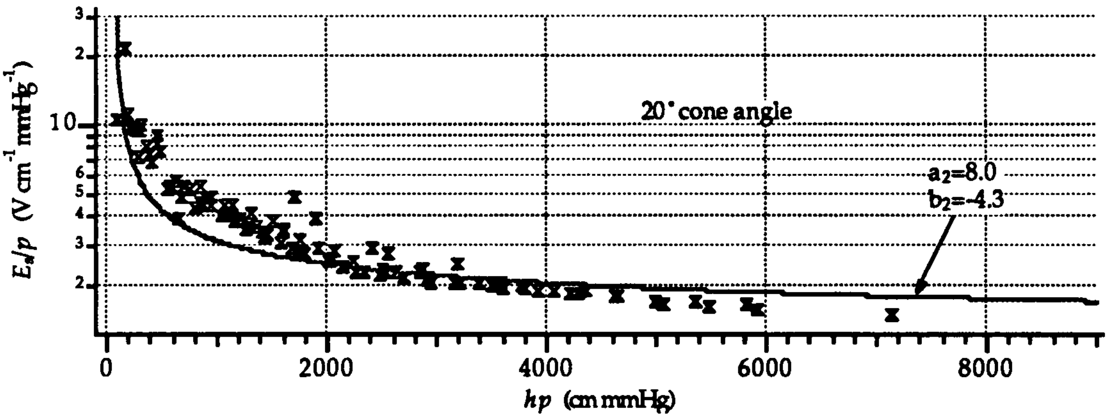

(b)

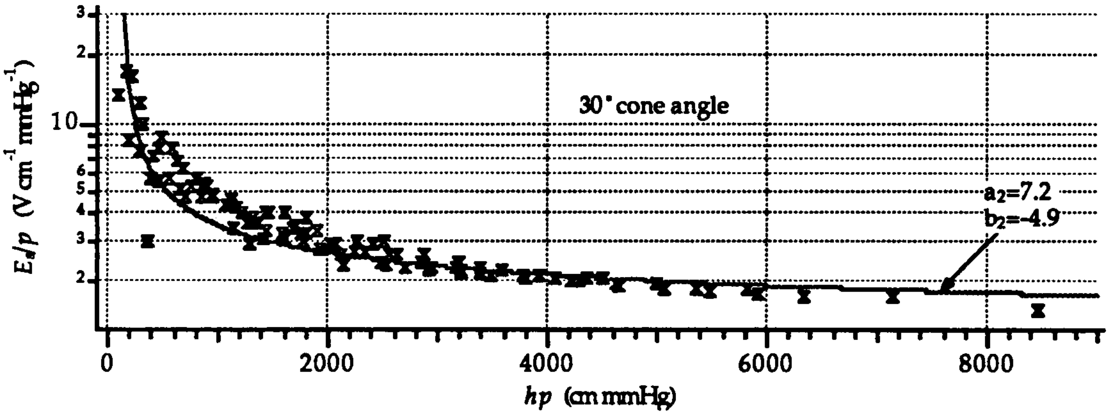

(c)

Figure 4.6. Critical field strengths vs. *hp* for each of the eight pins.

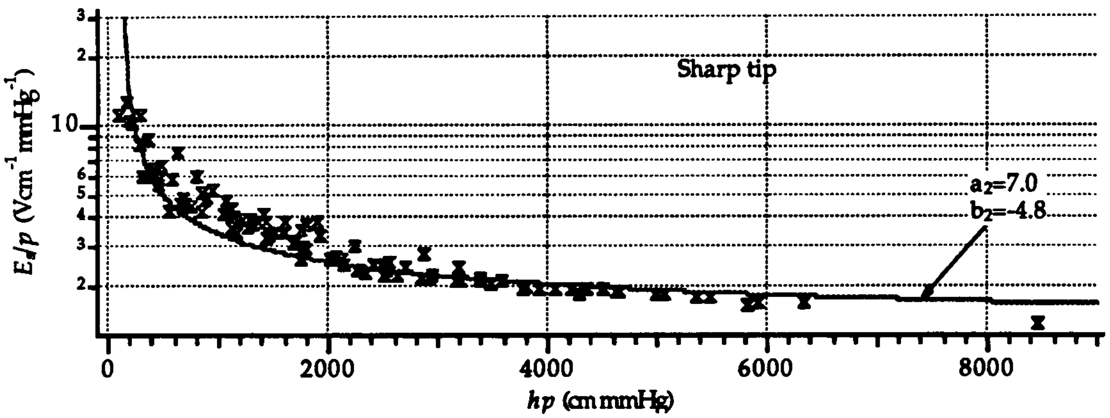

(d)

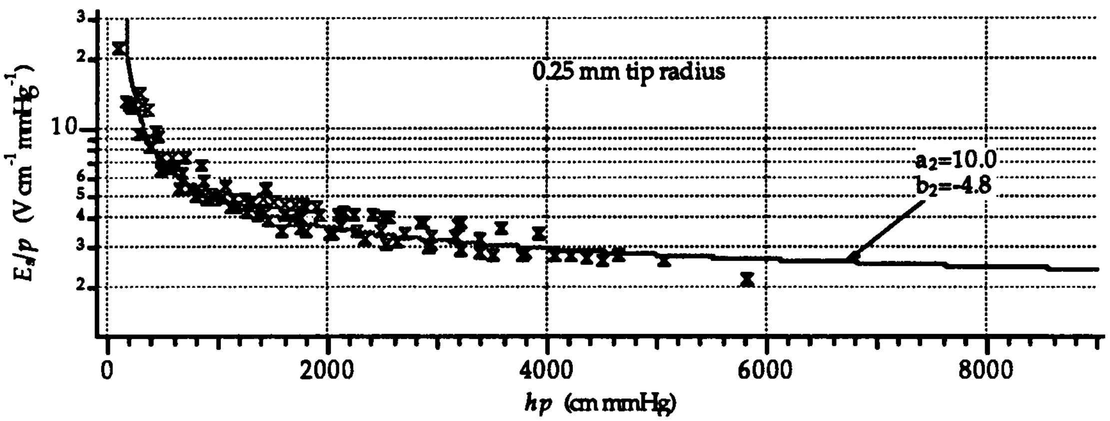

(e)

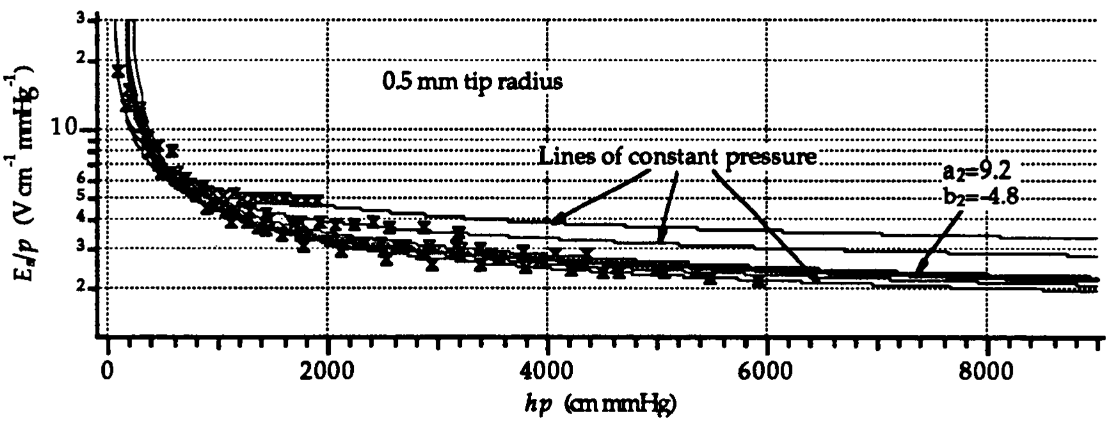

(f)

Figure 4.6 (continued)

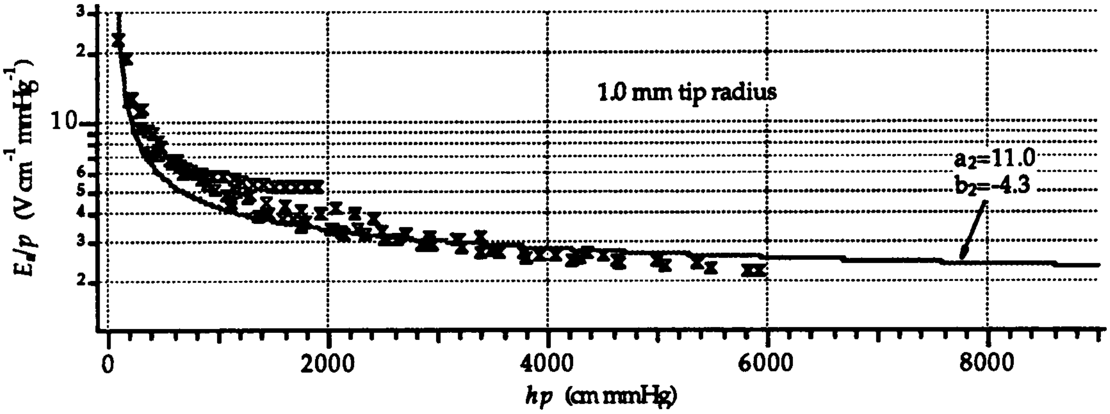

(g)

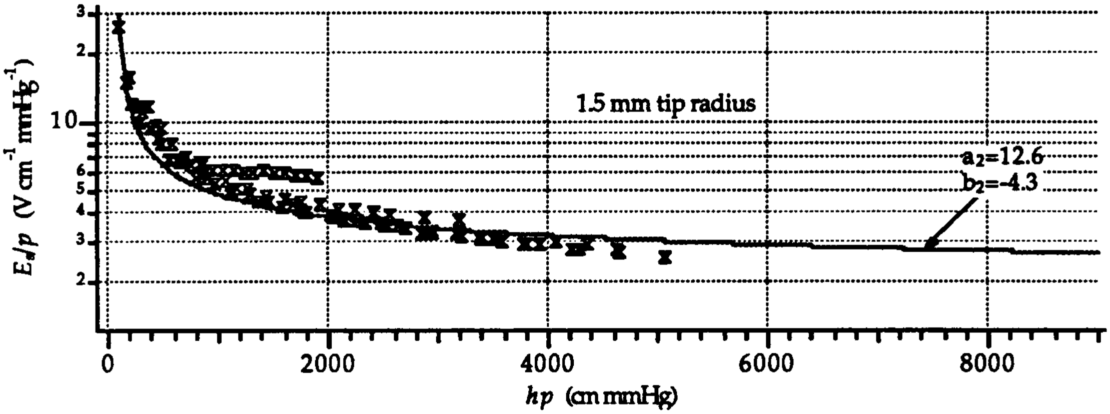

(h)

Figure 4.6 (continued)

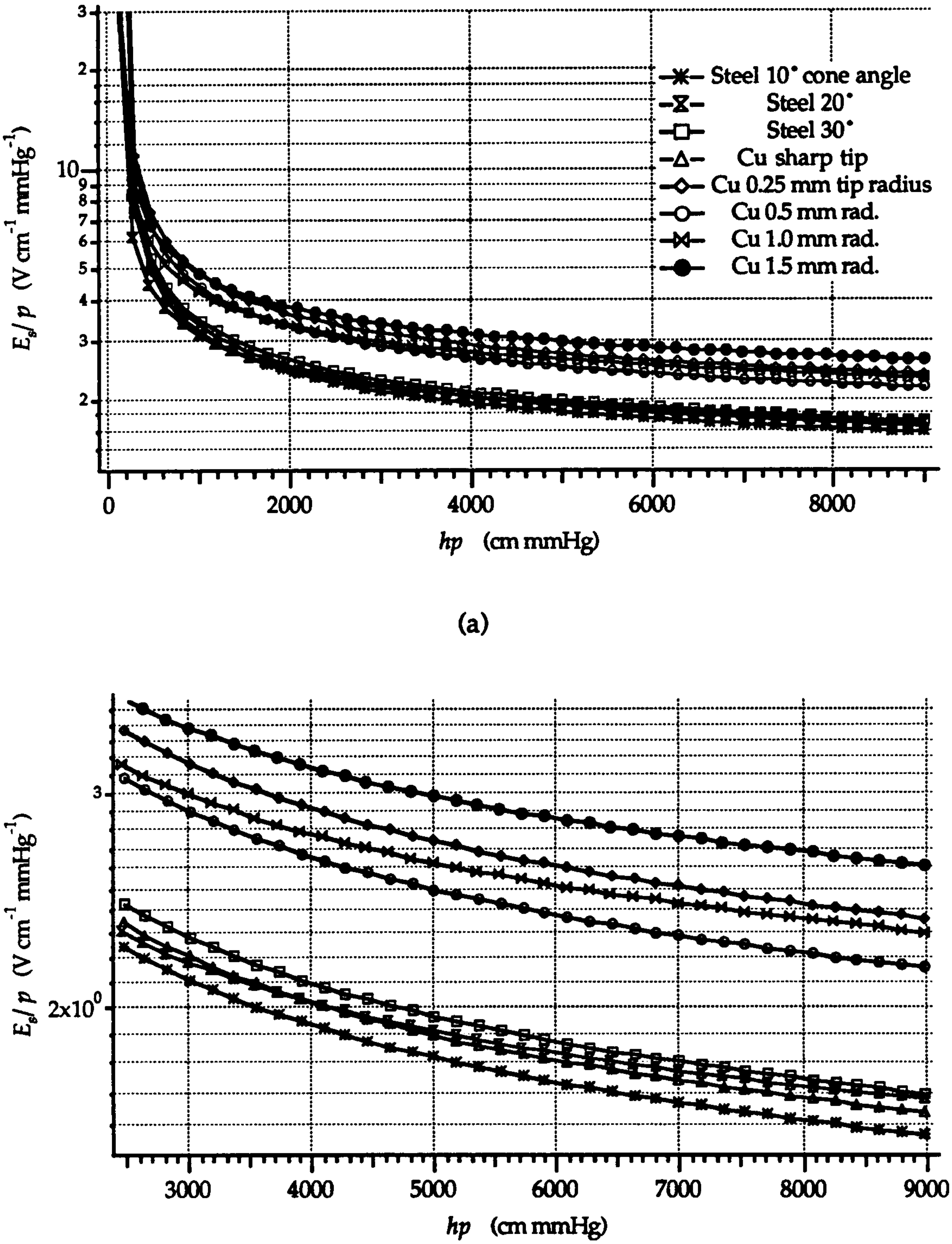

(a)

(b)

Figure 4.7. Curve fits of critical field strength to Equ. 4.2 for all eight pins.

with 4.7(a) showing the full range and 4.7(b) expanded to show the variation at higher values of hp. Although the curves for the four sharp pins are grouped very closely together, there is a noticeable increase in critical field strength with increasing cone angle for the steel pins. The same thing occurs in general for the copper pins with increasing tip radii, but with the 0.25 mm pin being another exception.

Breakdown Voltage

Since the coronal threshold voltage has been seen to have only a small dependence on pressure for the larger tip radii, an investigation was conducted to find out whether or not the same dependence holds true for the complete breakdown voltage V_b. Figure 4.8 shows V_b plotted against the product of gap size and pressure, hp, for each of the eight pins. Points in the shaded regions are those for which the discharge passed directly from the Townsend phase to the arc phase without forming a corona, and because of this fact, should therefore be considered as threshold voltages and not as breakdown voltages.

It seems fairly clear from these figures, apart from those points in the shaded regions, that the breakdown voltage is a linear function of the product of gap size and pressure,

$$V_b = a_3 hp + b_3, \tag{4.3}$$

where the parameters a_3 and b_3 are functions of pressure and tip geometry. Figure 4.9 shows the values of a_3 and b_3 resulting from linear fits to the data in Figure 4.8 plotted against the pressure. A very good approximation results when b_3 is assumed to have a linear dependence on pressure as $b_3 = k_0 - k_1 p$,

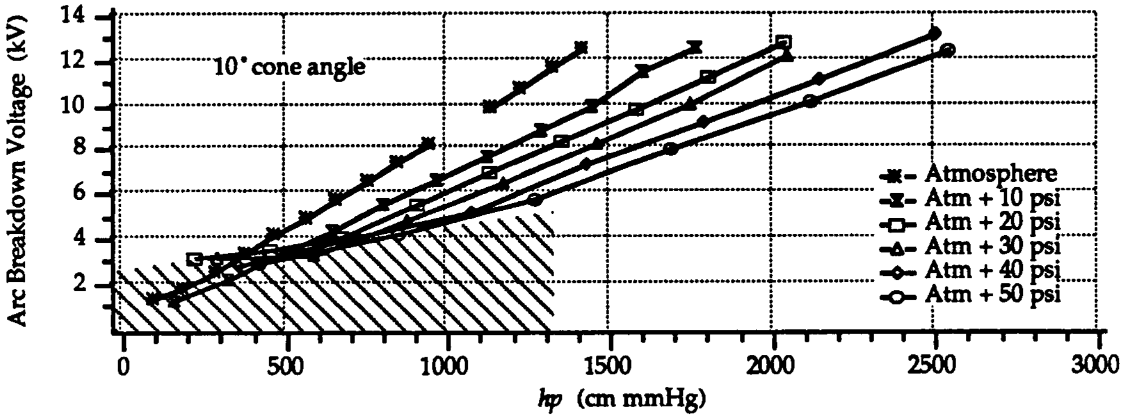

(a)

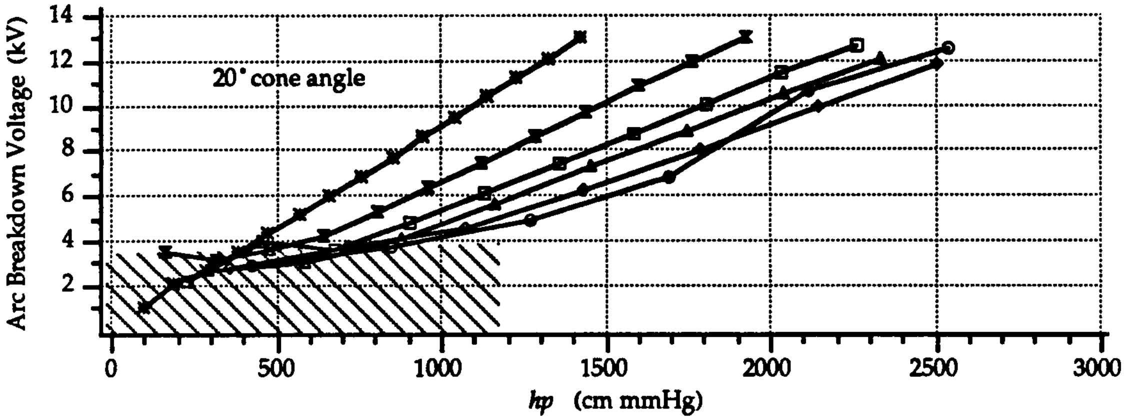

(b)

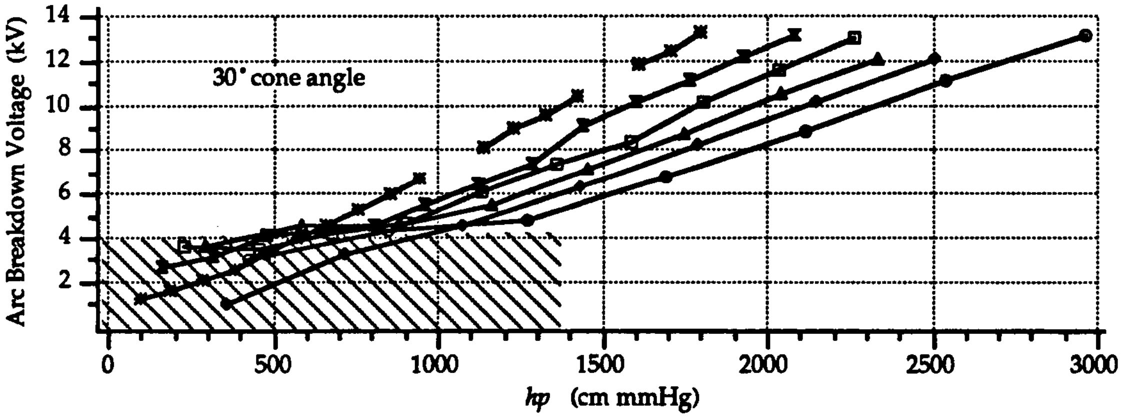

(c)

Figure 4.8. Breakdown voltage vs. *hp* for all eight pins.

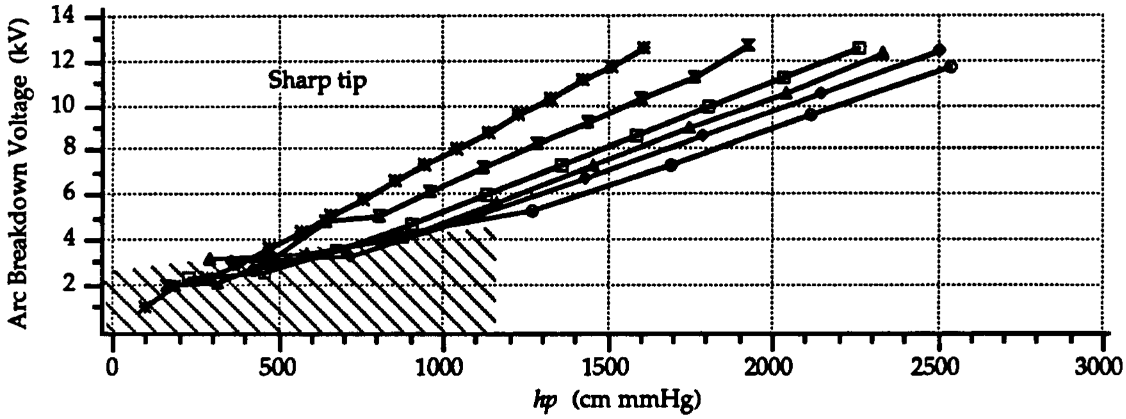

(d)

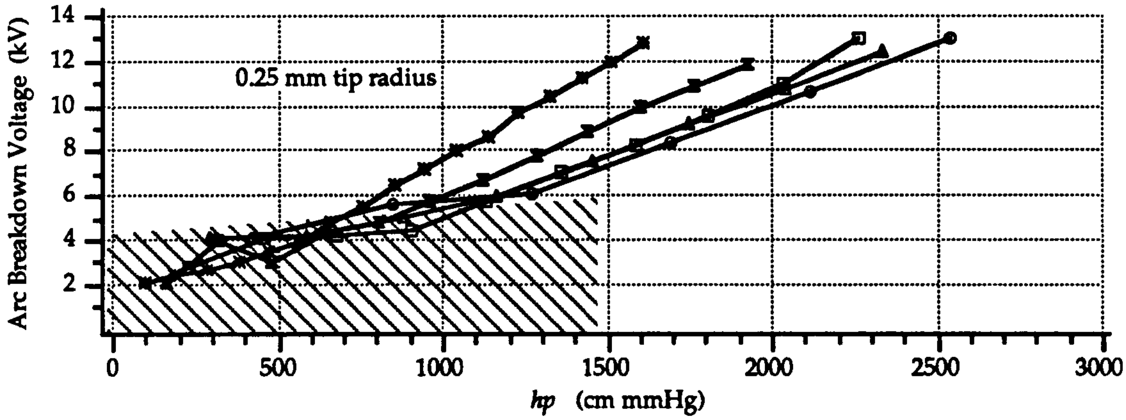

(e)

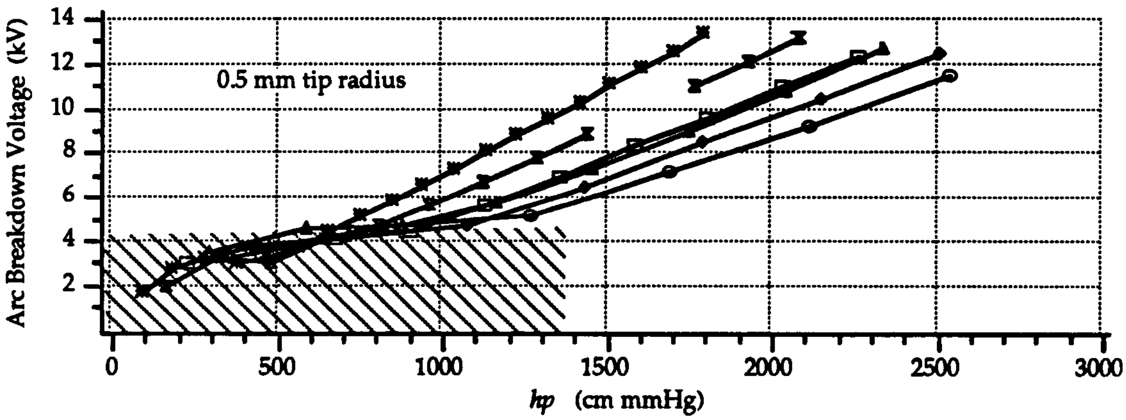

(f)

Figure 4.8 (continued)

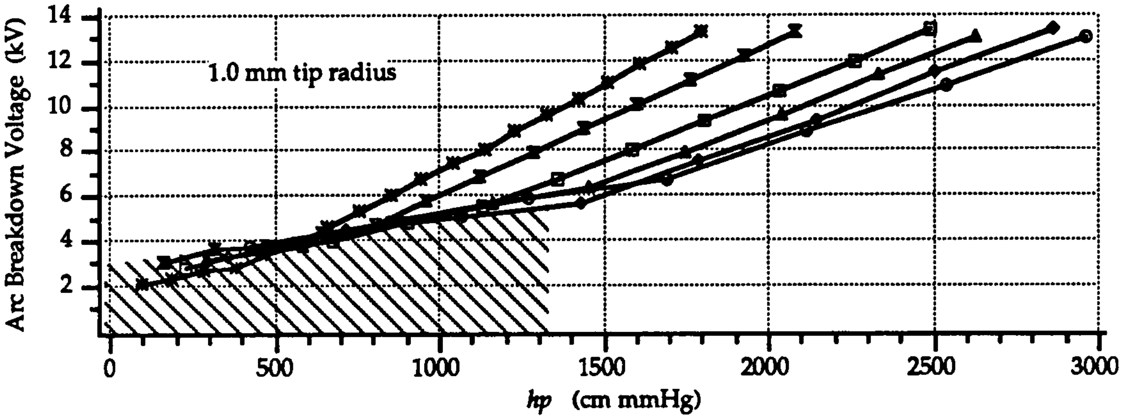

(g)

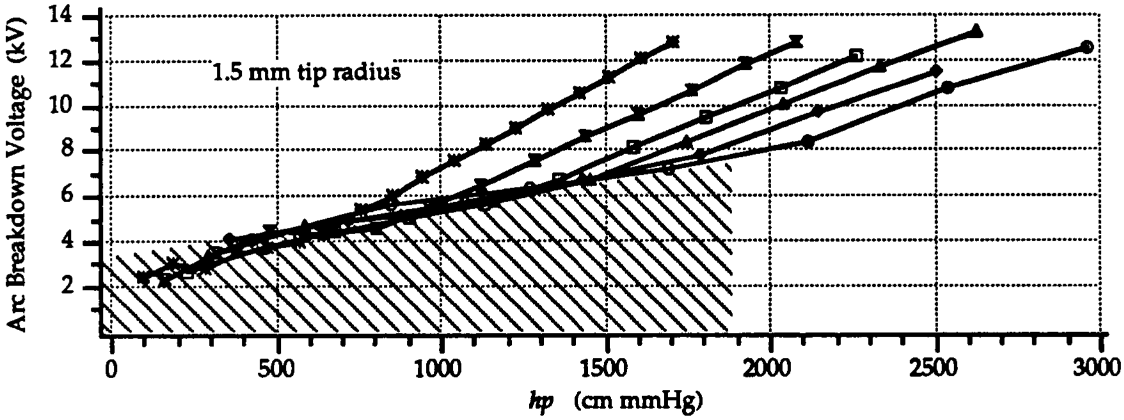

(h)

Figure 4.8 (continued)

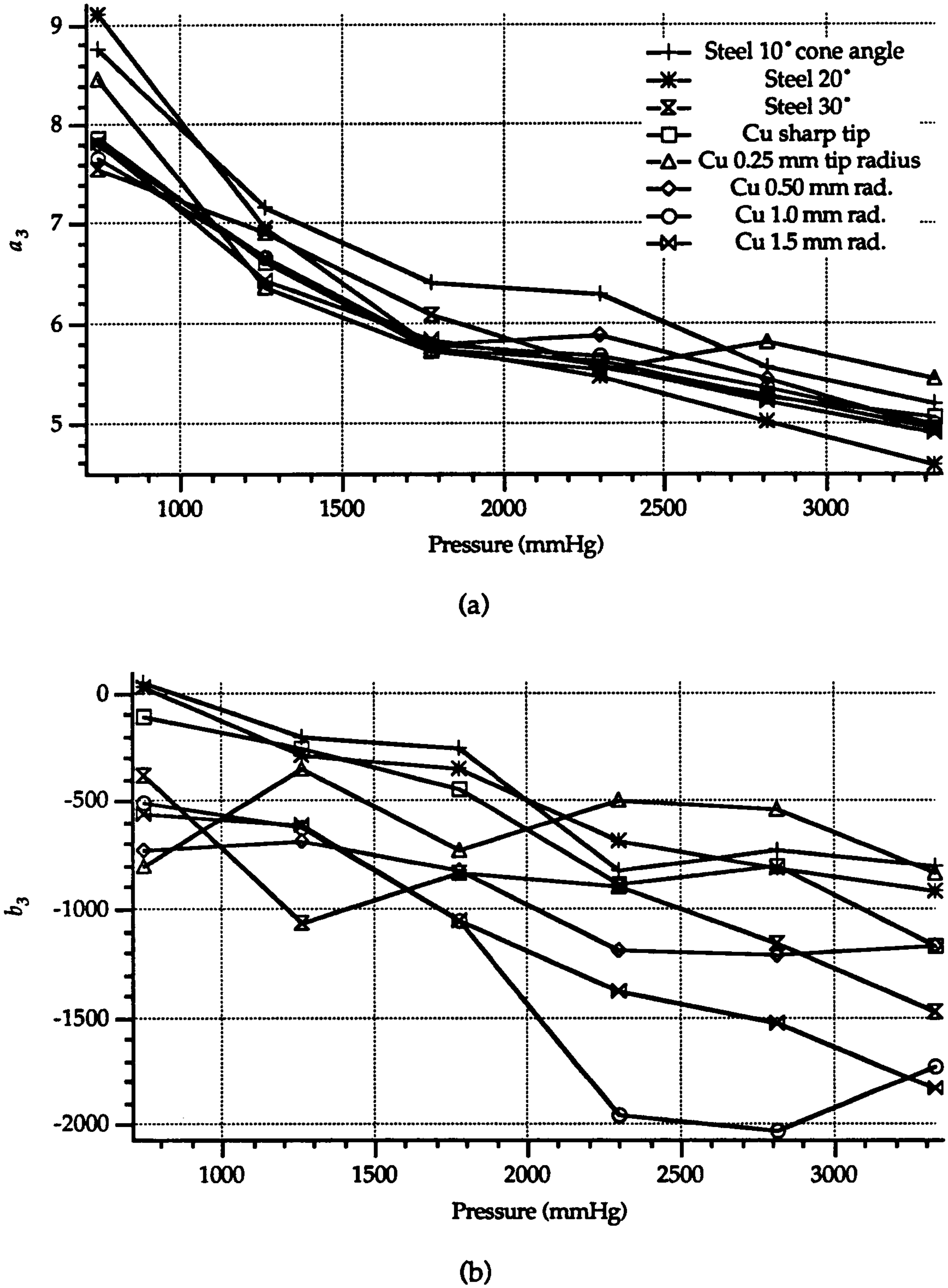

Figure 4.9. Slope (a) and intercept (b) of curve fits to V_b vs. hp.

and a_3 is taken to be an exponential function of pressure as

$$a_3 = k_2 + k_3 e^{-\left(\frac{p}{k_4}\right)}. \tag{4.4}$$

The breakdown voltage then assumes an empirical relation of the form

$$V_b = k_0 - k_1 p + \left(k_2 + k_3 e^{-\left(\frac{p}{k_4}\right)}\right) hp. \tag{4.5}$$

The values for k_i resulting from this type of approximation for each of the eight pins are listed in Table 4.1. As an example of the quality of the approximation, Figure 4.10 shows the arc breakdown data of Figure 4.8(d), the sharp copper pin, along with the curves obtained from Equation 4.5 using the appropriate values for k_i from Table 4.1. For any value of pressure and gap spacing, this equation and table give a value for the arc breakdown voltage, V_b, that in general can be expected to be accurate to ± 300 Volts.

Table 4.1. Values for the Empirical Constants k_i in Equation 4.5.

Pin	k_0	k_1	k_2	k_3	k_4
St 10 deg	264	.354	4.92	7.04	1190
St 20 deg	246	.368	4.52	10.9	858
St 30 deg	-312	.321	3.83	5.38	2100
Cu sharp	224	.409	4.97	6.67	895
Cu .25	-570	.027	5.58	19.6	390
Cu .5	-497	.231	4.87	5.65	1110
Cu 1.0	-54.6	.619	4.80	5.42	1160
Cu 1.5	-99.7	.521	4.82	6.36	971

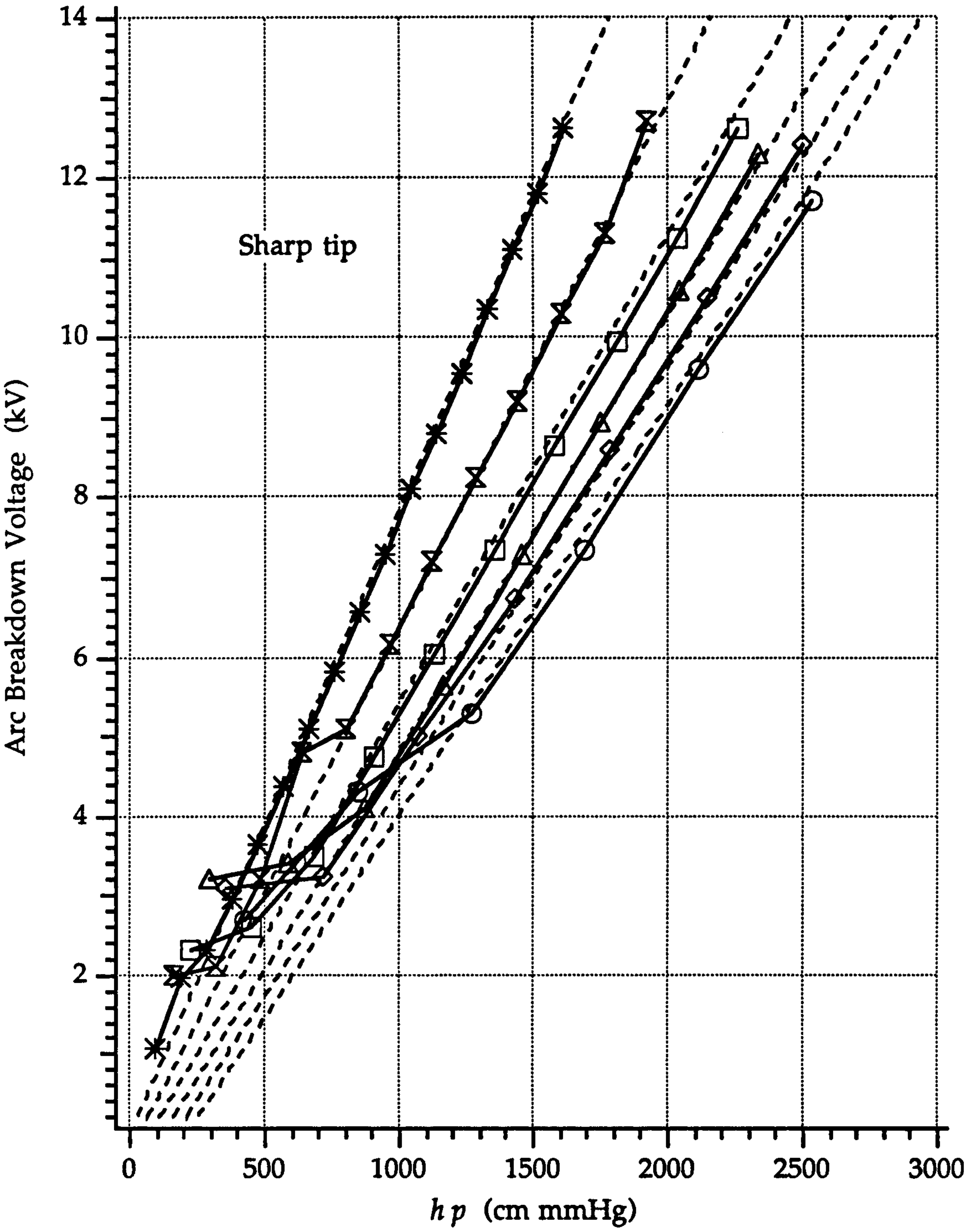

Figure 4.10. Breakdown voltage for the sharp copper pin with predicted curves from Equation 4.5.

Shape of the Coronal V-I Curve

In Chapter 3 it was put forward that the voltage-current characteristics of the corona phase of the electrical discharge might be described by the relation given by Equation 3.18. Here, V_s was supposed to be the threshold voltage for formation of the corona, while C was a parameter dependent on gas type, gap spacing, and pressure. In an effort to verify this equation, each of the coronas at every step of pressure and gap spacing for which all three discharge phases occurred was fit to a parabolic equation of the form

$$i_G = c_1 V_G (V_G - c_2) \tag{4.6}$$

The values for the parameters c_1 and c_2 that were obtained from these fits were plotted against the gap spacing and analyzed to determine how they varied with changes in both gap spacing and pressure. In order to illustrate this process, the 1.5mm copper pin has been chosen as being representative of the results from the other pins and will, therefore, serve as the example. Figure 4.11 shows the two parameters c_1 and c_2 plotted vs. gap spacing for the 1.5mm copper pin.

It is apparent from the logarithmic plot of Figure 4.11(a), that c_1 may be approximated by an exponential function. A completely general exponential function may be written as

$$c_1 = k_0 + e^{k_1 - \beta h}. \tag{4.7}$$

A curve fit of each of the lines in Figure 4.11(a) to Equation 4.7 results in a value of k_0, k_1, and β for each step in pressure. Figure 4.12 shows these three parameters plotted against pressure. Figure 4.12(a) shows k_0 varying over only a very small range, and so may be assumed to be a constant equal to the average over all pressures. Now, the plot of k_1 is similar to that of k_0, and

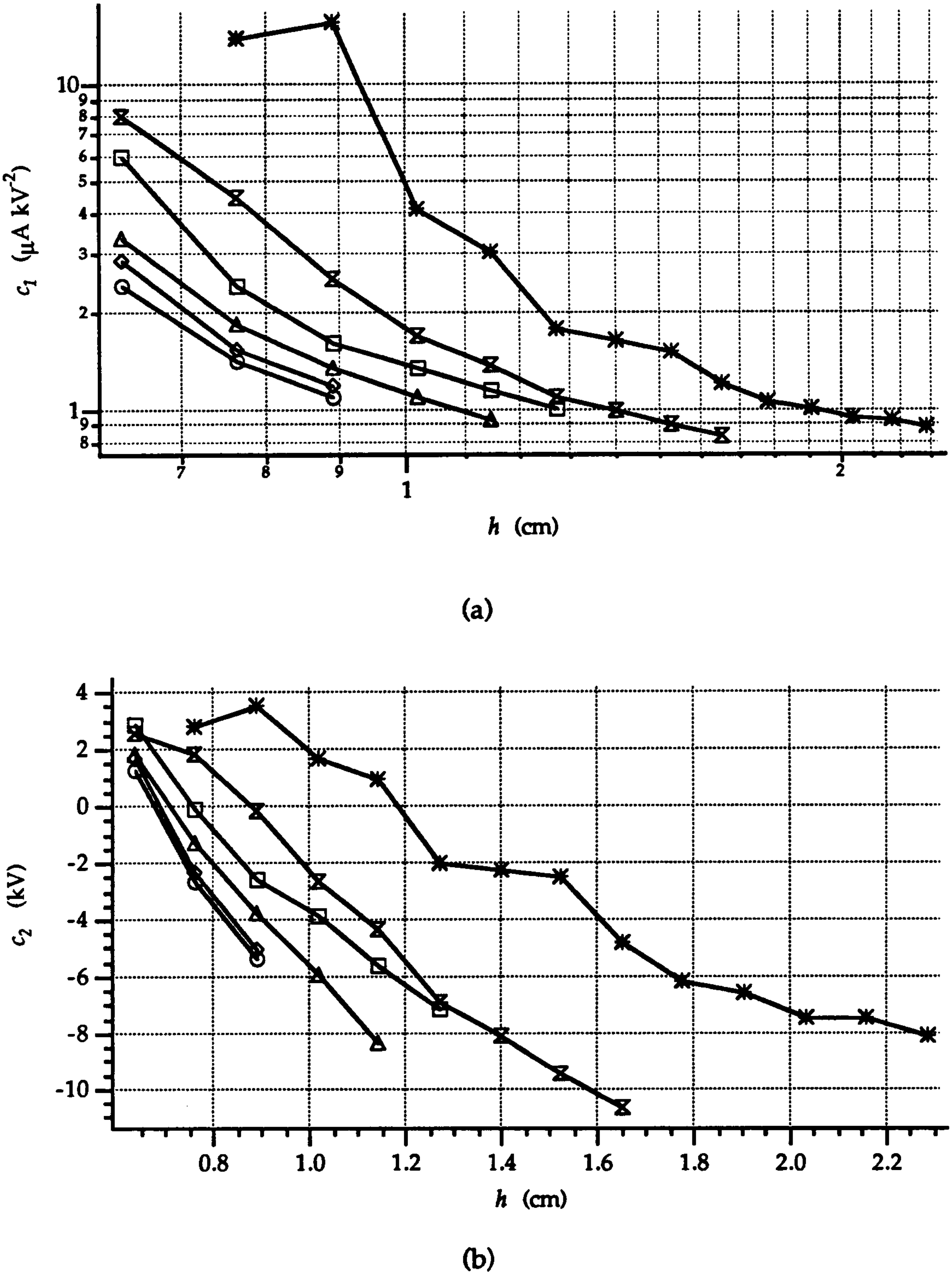

Figure 4.11. Parameters c_1 (a) and c_2 (b) from fit of coronas to Equation 4.6 for the 1.5 mm copper pin.

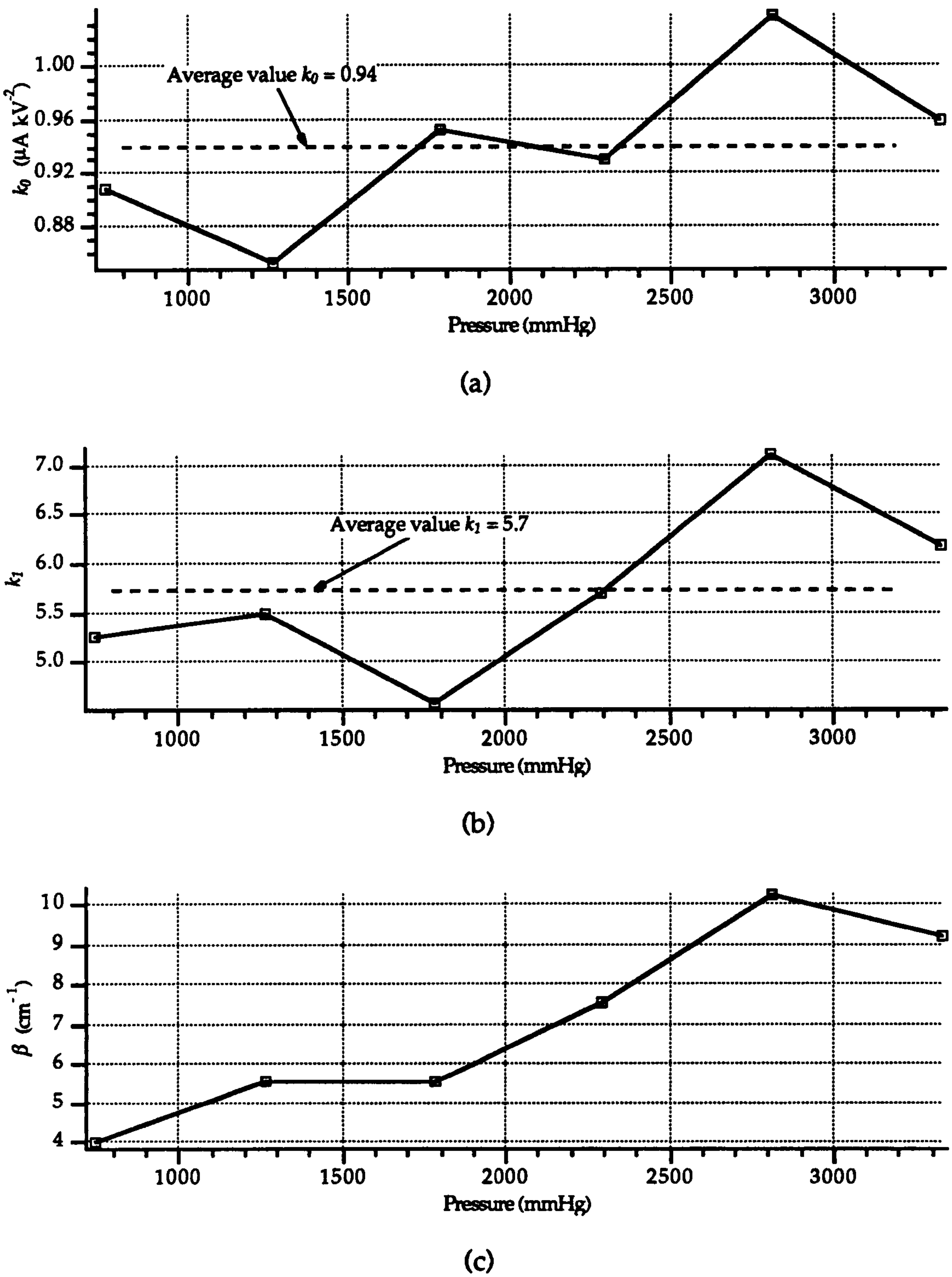

Figure 4.12. The parameters k_0 (a), k_1 (b) and β (c) resulting from curve fits of c_1 to Equation 4.7 for the 1.5 mm copper pin.

since k_1 is related to the intercept on the h=0 axis, changes of the order shown will only have a small affect on the actual shape of the curve, allowing k_1 also to be approximated by an average value.

The dependence of β on pressure, however, is more subtle. The values for β shown in Figure 4.12(c) were obtained from a curve fit in which all three parameters were allowed to vary, and the resulting shape of the curve provides no insight into the form for β . If, instead, k_0 and k_1 were fixed at their average values and only β were varied during a second fit, a clear exponential dependence surfaced. Figure 4.13 shows these values for β resulting from this second fit plotted against pressure along with the exponential curve that they follow. Substituting the exponential form of β into Equation 4.7 gives the following expression for c_1:

$$ln(c_1 - k_0) = k_1 - h\left(k_2 - k_3 e^{-p/k_4}\right). \tag{4.8}$$

Now the parameter c_2, as shown in Figure 4.11(b), looks as though its dependence on h is approximately linear. Linear fits to those curves of the form

$$c_2 = \eta_1 + \eta_2 h \tag{4.9}$$

result in values for η_1 and η_2 at each pressure setting. These parameters themselves turn out to follow a nearly linear variation with pressure. Figure 4.14 shows the values of η_1 and η_2 resulting from linear fits to the curves in Figure 4.11(b), along with their own linear approximations. The parameter c_2 then takes the form

$$c_2 = m_0 + \frac{p}{m_1} - h\left(m_2 + \frac{p}{m_3}\right). \tag{4.10}$$

So it appears that the parameter c_2 does not correspond here to the threshold

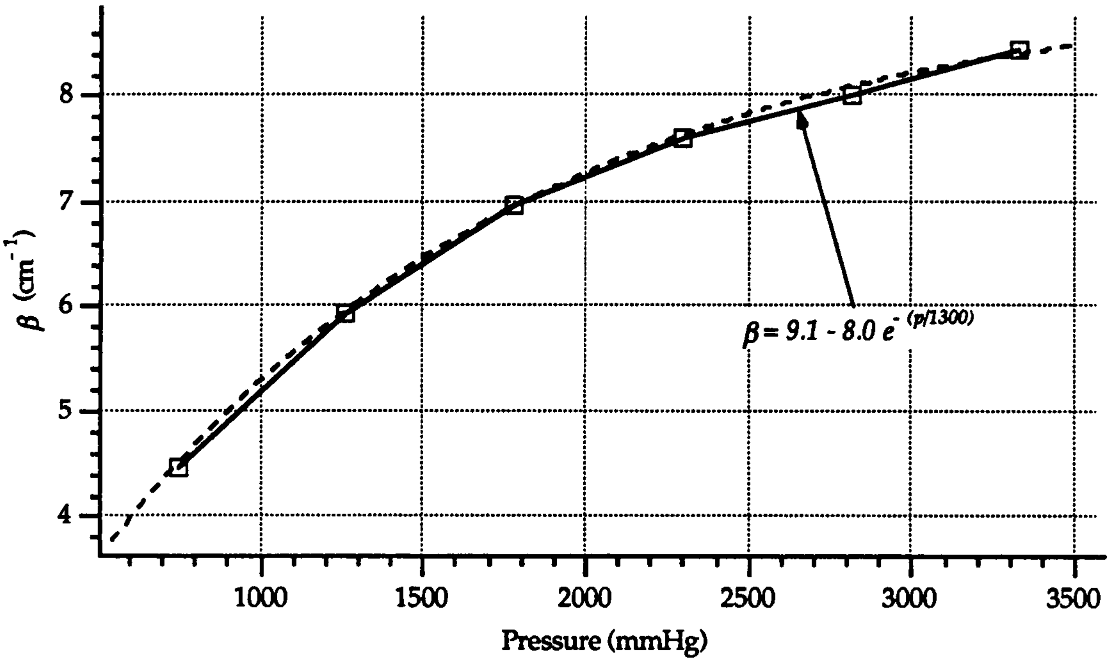

Figure 4.13. Values of β resulting from fit with k_0 and k_1 held constant.

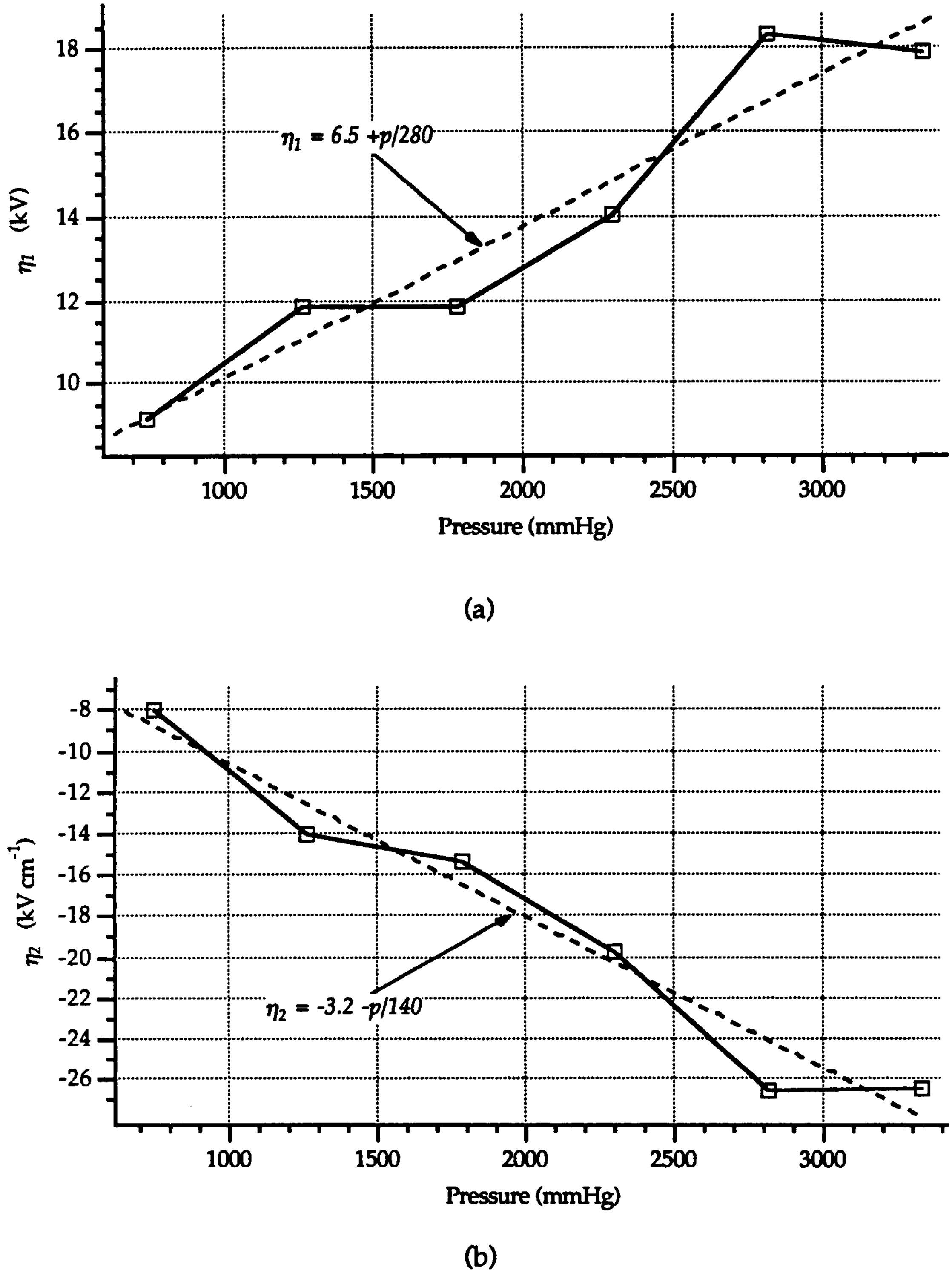

Figure 4.14. The parameters η_1 (a) and η_2 (b) resulting from curve fits of c_2 to Equation 4.9 for the 1.5 mm copper pin.

voltage V_s since, first of all, it is negative, and secondly, it is strongly dependent on h and p individually as well as on their product.

When taken together, Equations 4.8 and 4.10, along with the empirical values for the k_i and m_i, give approximate values for the parameters c_1 and c_2 for any gap spacing or pressure in the range studied here. Table 4.2 lists the values for the constants k_i for the 1.5 mm copper pin as well as those obtained for the rest of the pins. Table 4.3 gives the values of m_i obtained from this analysis for each of the eight pins. Continuing with the 1.5mm copper pin as the representative example, Figure 4.15 illustrates the quality of the approximations for c_1 and c_2 obtained by using Equations 4.8 and 4.10.

Shape of the Arc V-I Curve

Equation 3.35 from Chapter 3 indicates that the voltage across the arc for constant pressure will be a function of the current following the form

$$V_G = c_3\, i_G^{-n}, \tag{4.11}$$

where the parameter c_3 would depend on the gap size. The shape of the V-I curve in the arc region was obtained in much the same way as in the coronal regime. Every arc for which all three discharge phases occurred was fit to Equation 4.11. The parameters c_3 and n are not independent, however, so the first set of results for n were averaged at each pressure setting, and the curve fits were done again varying only c_3 while holding n fixed at its average value.

Figure 4.16 shows these values of n and how they varied with pressure and tip geometry for both the steel and copper sets of pins. Figure 4.16(a) indicates that for the steel pins the parameter n decreased in general with

Table 4.2. Values for the Empirical Constants k_i in Equation 4.8.

Pin	k_0	k_1	k_2	k_3	k_4
St 10 deg	.735	2.94	7.16	7.70	1070
St 20 deg	.673	3.09	8.30	6.52	2630
St 30 deg	.631	3.36	9.93	8.76	3420
Cu sharp	.808	2.60	11.2	9.86	5710
Cu .25	.704	3.88	15.2	13.6	5090
Cu .5	.768	3.79	12.6	11.7	3780
Cu 1.0	.705	4.16	11.4	8.99	4880
Cu 1.5	.940	5.72	9.06	8.03	1340

Table 4.3. Values for the Empirical Constants m_i in Equation 4.10.

Pin	m_0	m_1	m_2	m_3
St 10 deg	6.15	-2830	11.9	411
St 20 deg	4.61	901	5.73	184
St 30 deg	5.40	538	3.34	135
Cu sharp	3.23	1080	3.12	181
Cu .25	6.32	667	3.82	143
Cu .5	4.36	535	1.35	158
Cu 1.0	5.47	407	3.02	171
Cu 1.5	6.47	276	3.21	135

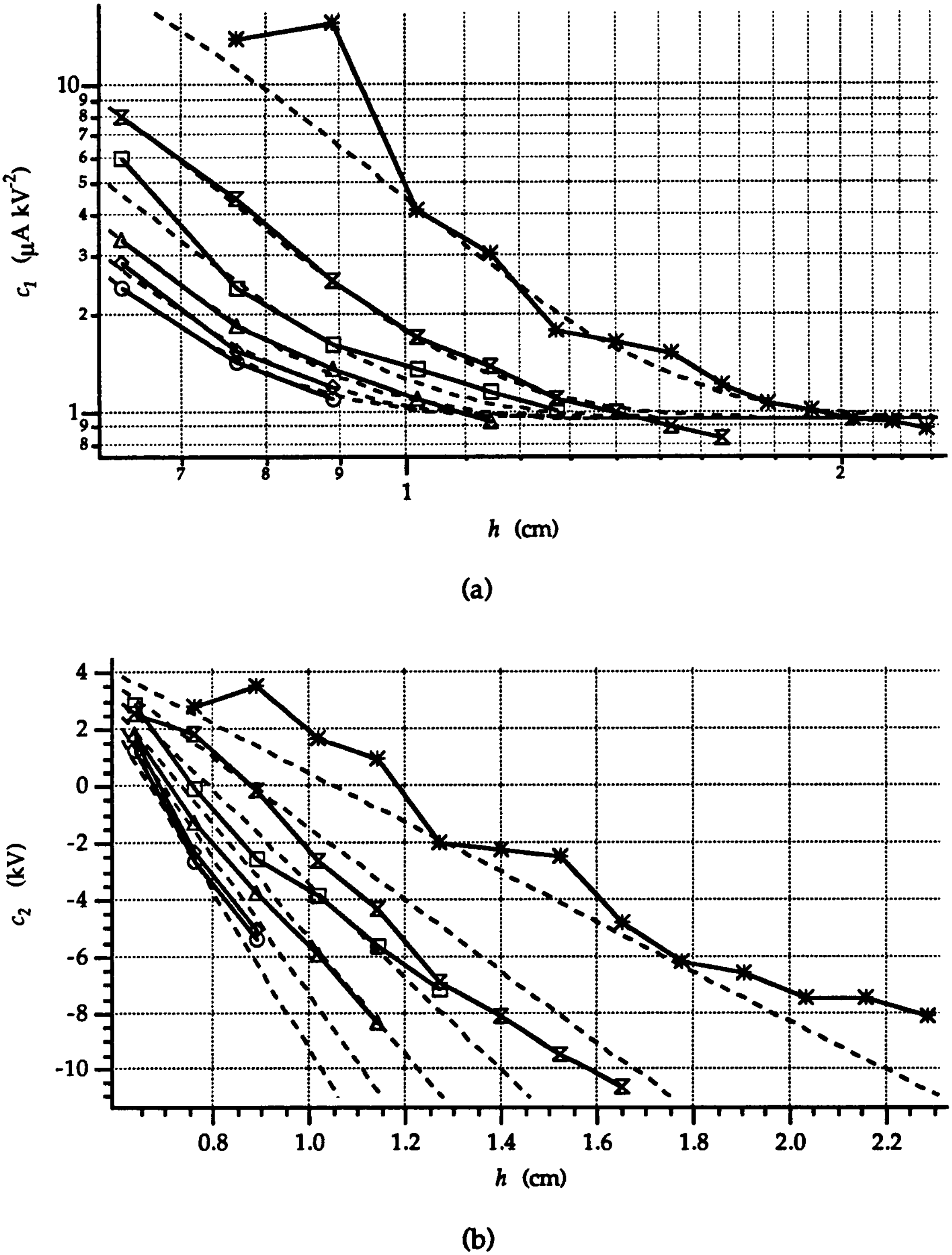

Figure 4.15. Parameters c_1 (a) and c_2 (b) with predicted curves from Equations 4.8 and 4.10 respectively, for the 1.5 mm copper pin.

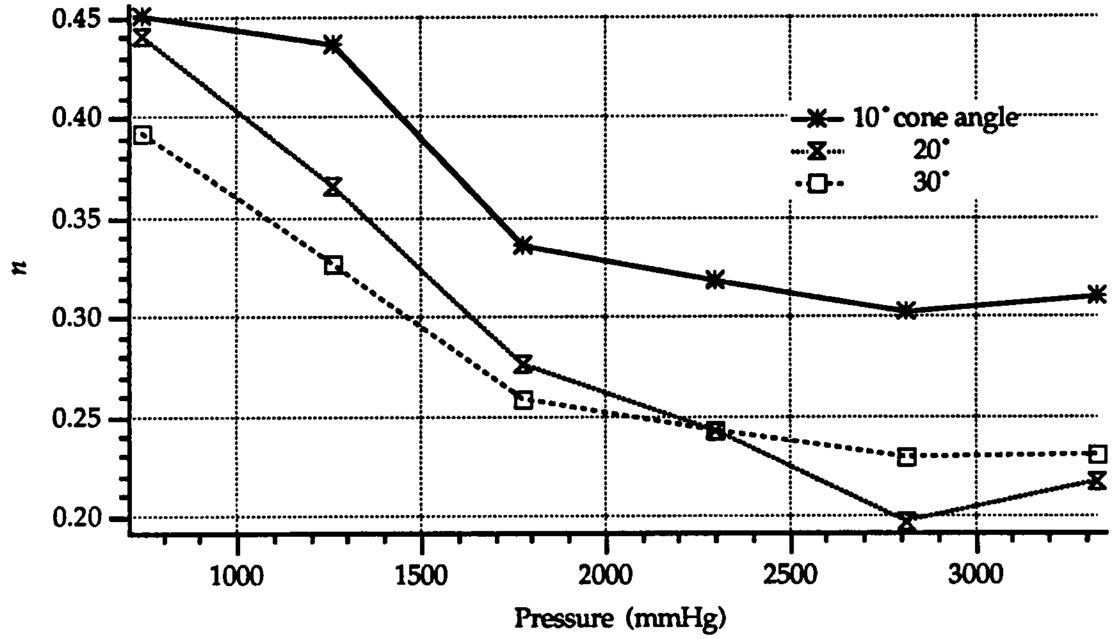

(a)

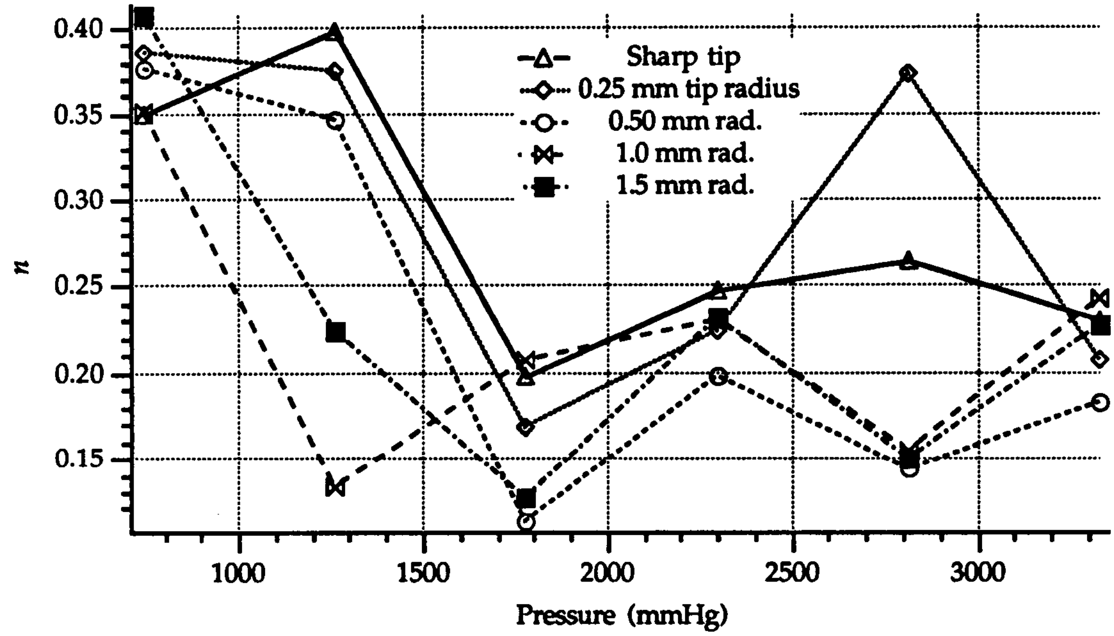

(b)

Figure 4.16. Variation of the average values for *n* of Equation 4.11 for the steel (a) and copper (b) pins.

increasing cone angle, while for the copper pins in Figure 4.16(b), it is apparent that the same effect occurred for increasing tip radii, although it is not as clear as for the steel pin case. These graphs also show a general decrease in n for increasing pressure in both sets of pins. But, aside from this general trend, very little more can be determined about the dependence of n on pressure. One other item of note from Figure 4.16 is the observed range of n. In the derivation of Equation 3.35 it was predicted that n would lie in the range $.45 < n < .89$, but here n is observed to lie noticeably lower than this, in the range $.11 < n < .45$.

Figure 4.17 shows, for each of the eight pins, the values of c_3 resulting from the curve fits to Equation 4.11 with n held fixed at each pressure. Each of these graphs exhibits a linear dependence on the gap size h for every pressure so that c_3 may be written as

$$c_3 = \eta_3 + \eta_4 h. \tag{4.12}$$

Linear approximations to each of the curves in any of the graphs of Figure 4.17 result in values of η_3 and η_4 for each pin type and pressure. As an example, Figure 4.18 shows these values as functions of pressure for the case of the 1.5 mm Copper pin. Notice the similarity between the graphs of η_3 and η_4 in this figure with the curve for n of that pin in Figure 4.16. This indicates that η_3 and η_4 depend on the pressure only through n. Insight into the nature of this dependence is provided by plotting the values for η_3 and η_4 against the corresponding values of n. This was done for each of the eight pins, and it was found that a good approximation to the dependence of η_3 and η_4 on n was given by a third order polynomial of the form

$$\eta_3 = k_0 + k_1 n + k_2 n^2 + k_3 n^3, \tag{4.13}$$

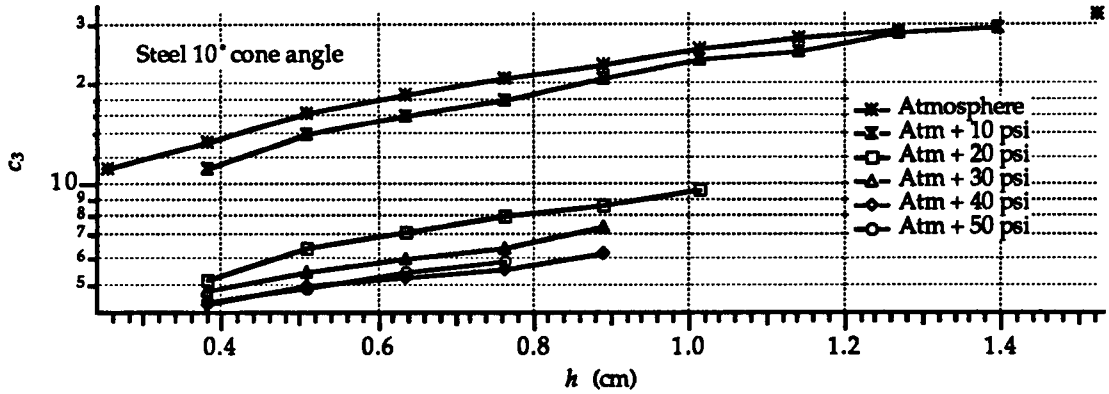

(a)

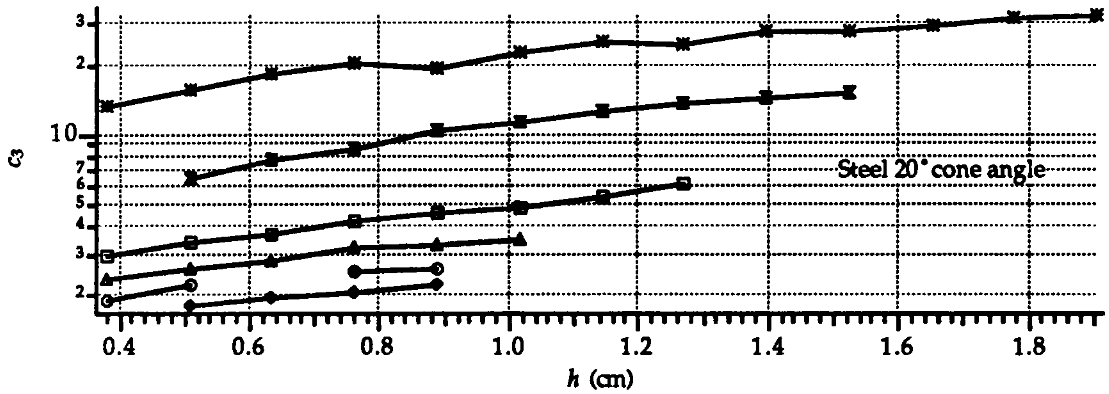

(b)

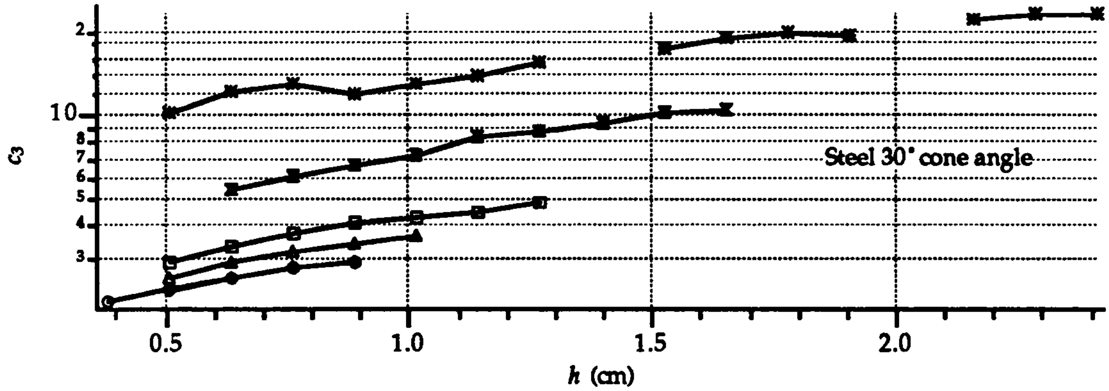

(c)

Figure 4.17. Parameter c_3 of Equation 4.11 resulting from curve fits of the arc region for all eight pins.

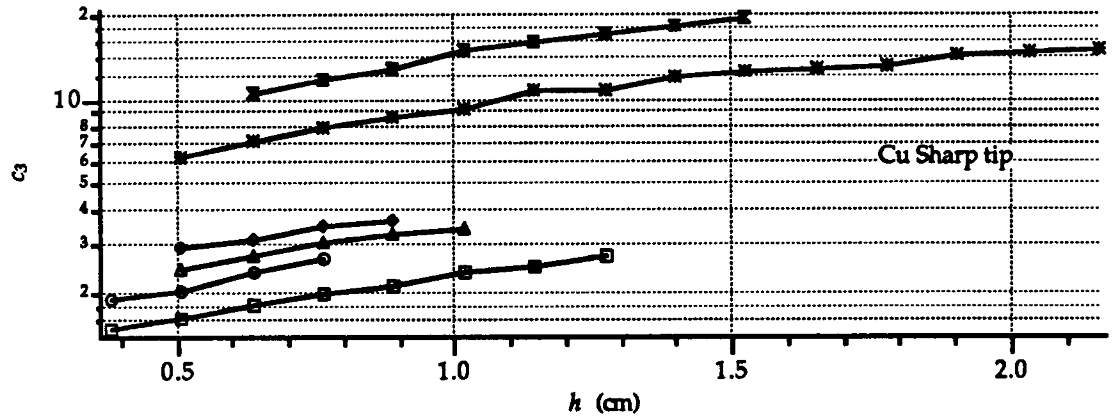

(d)

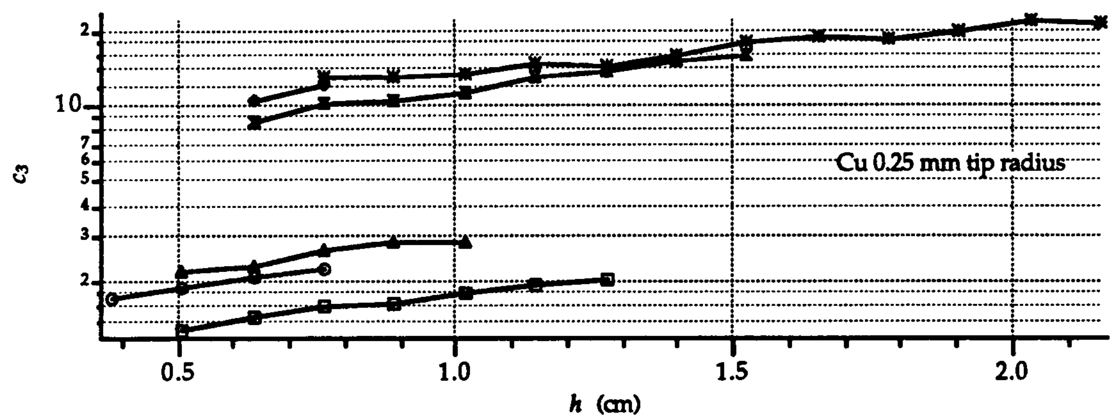

(e)

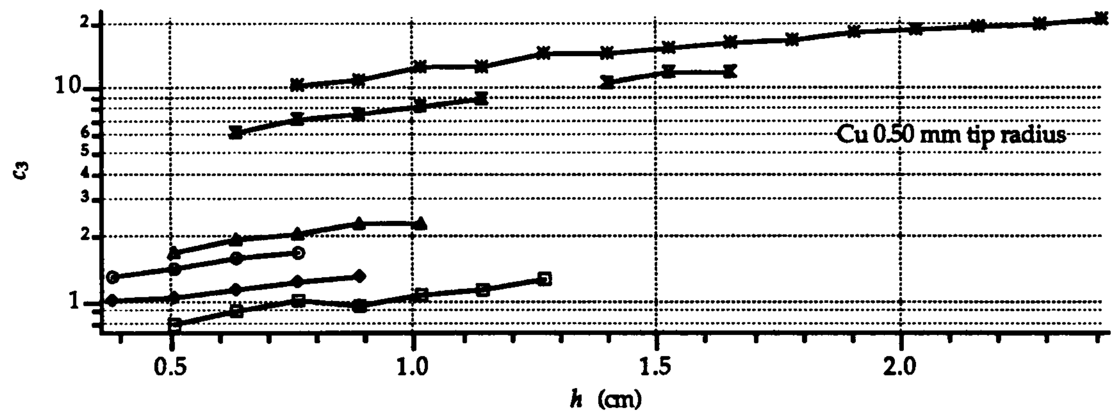

(f)

Figure 4.17 (continued)

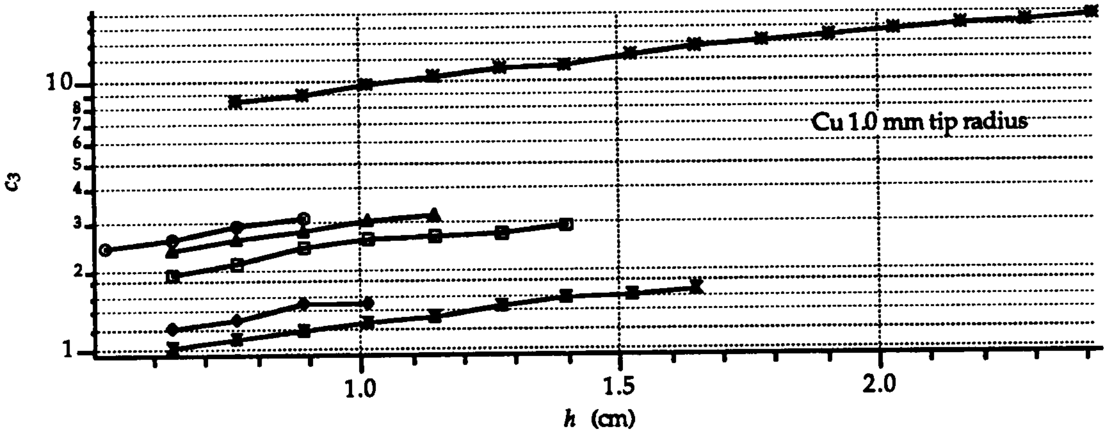

(g)

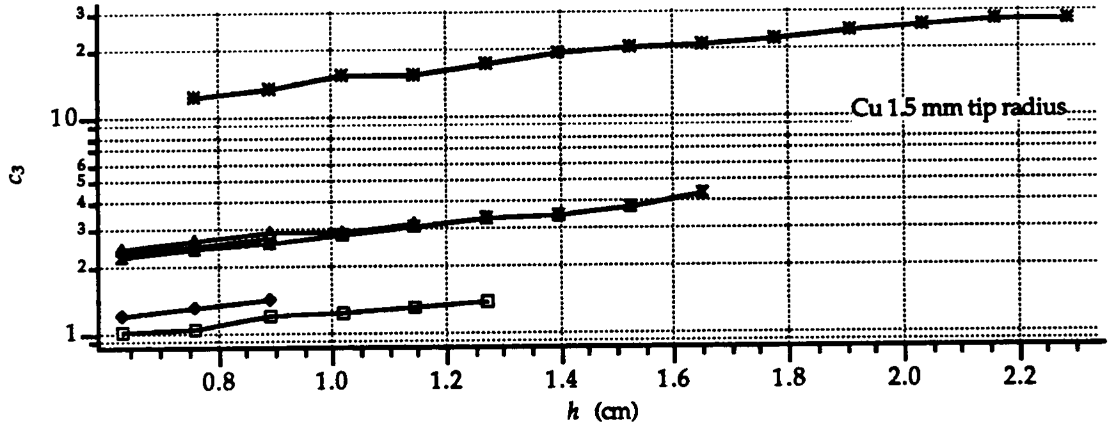

(h)

Figure 4.17 (continued)

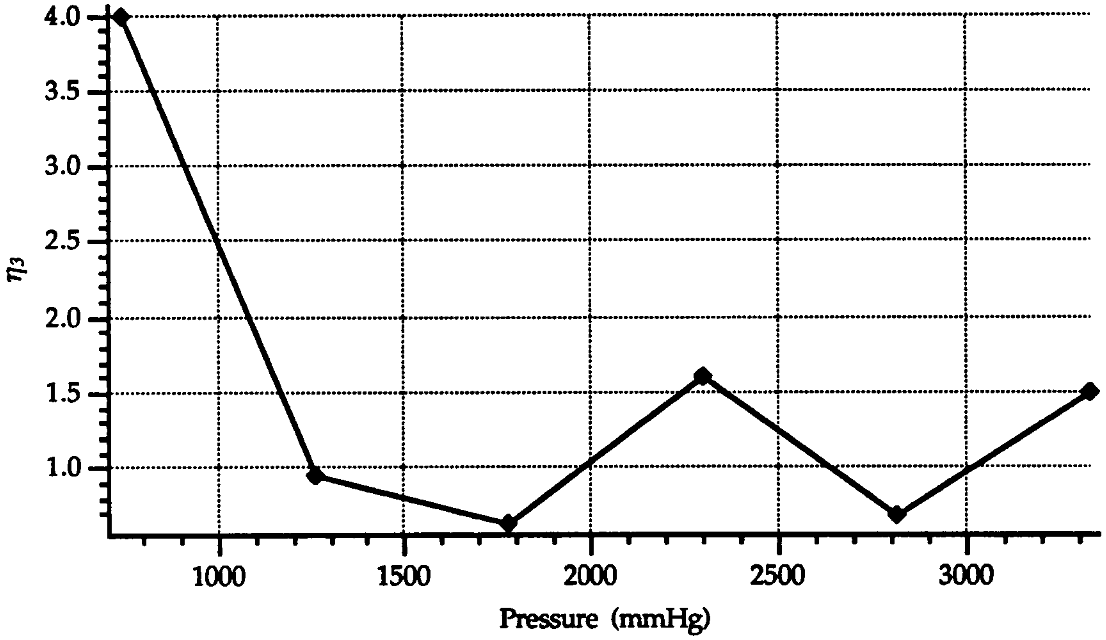

(a)

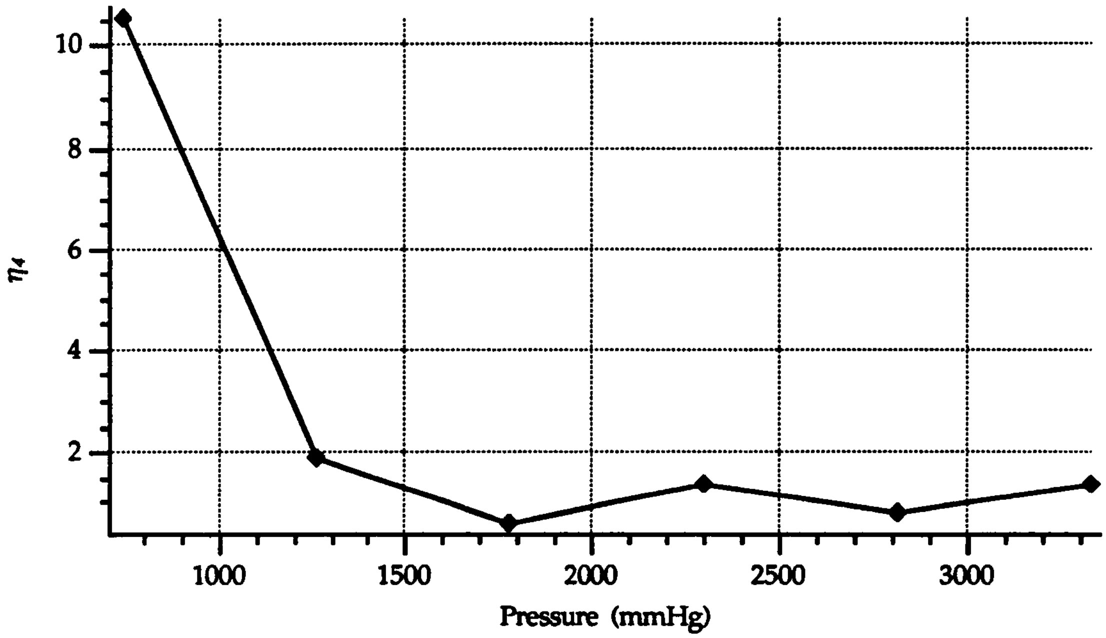

(b)

Figure 4.18. Values of the fit constants η_3 (a) and η_4 (b) of Equation 4.12 as functions of pressure for the 1.5 mm copper pin.

and similarly for η_4. The values of η_3 and η_4 as functions of n, along with their polynomial approximations given by Equation 4.13, are shown in Figure 4.19 for the case of the 1.5 mm copper pin.

With these relations for η_3 and η_4, Equation 4.11 can now be written showing the approximate dependence on h and n as

$$V_G = [(k_0 + k_1 n + k_2 n^2 + k_3 n^3) + h(k_4 + k_5 n + k_6 n^2 + k_7 n^3)] i_G^{-n}. \qquad (4.14)$$

Table 4.4 lists the values for the empirical constants k_i in Equation 4.14 for each of the eight pins. Figure 4.20 shows the values for c_3 and, again, in order to show their quality, the approximations obtained by using the values of k_i from Table 4.4 in Equation 4.14 are shown also.

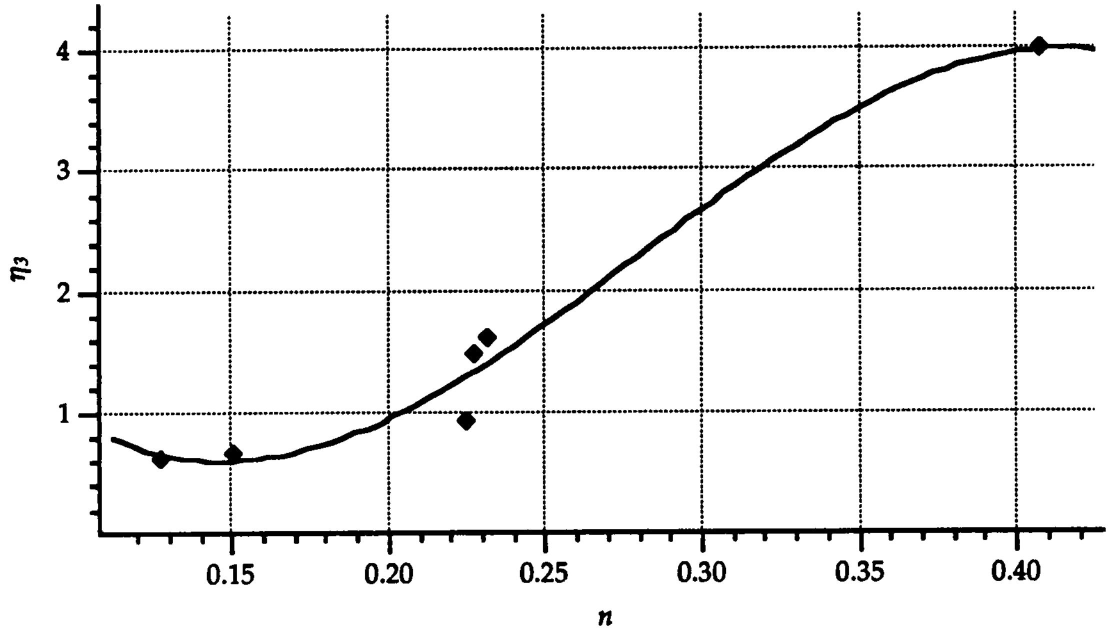

(a)

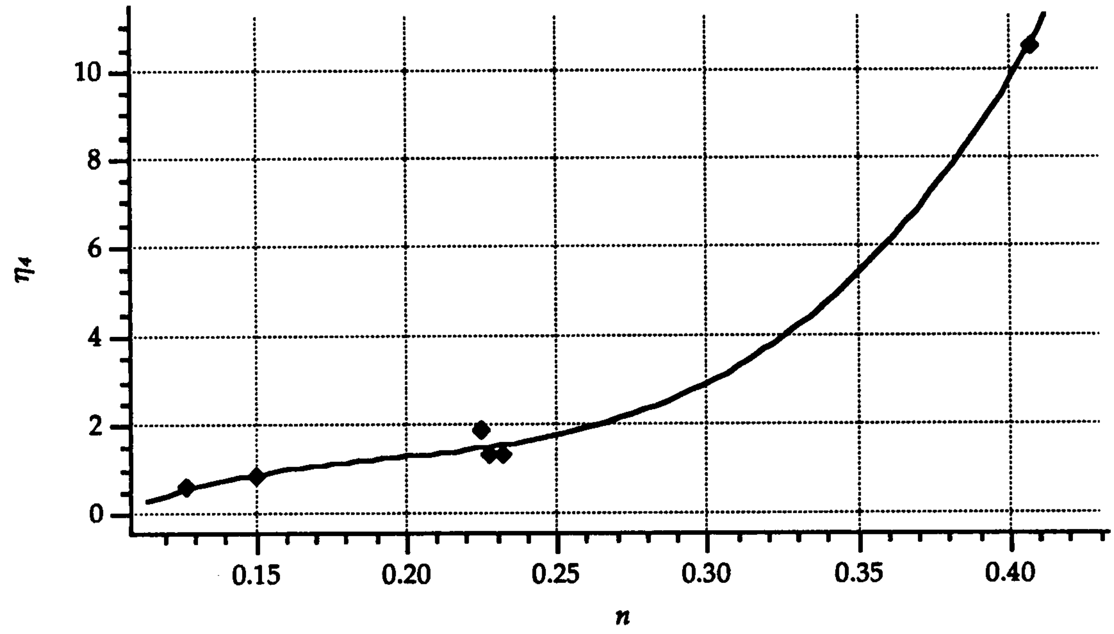

(b)

Figure 4.19. Values of the fit constants η_3 (a) and η_4 (b) of Equation 4.12 as functions of n for the 1.5 mm copper pin.

Table 4.4. Values for the Empirical Constants k_i in Equation 4.14.

Pin	k_0	k_1	k_2	k_3	k_4	k_5	k_6	k_7
St 10 deg	-.394	3460	-9950	9440	562	-4920	14100	-13000
St 20 deg	-38	445	-1650	2000	24	-271	972	-946
St 30 deg	-82.6	909	-3250	3860	45	-493	1770	-1950
Cu sharp	22.3	-260	997	-1150	-21.6	283	-1170	1660
Cu .25	-121	1580	-6580	8630	173	-2240	9280	11900
Cu .5	-13.2	224	-1120	1750	6.22	-95.4	468	-571
Cu 1.0	-2.78	49	-235	436	.337	3.51	-33.3	183
Cu 1.5	4.8	-64.6	298	-354	-6.17	101	-481	822

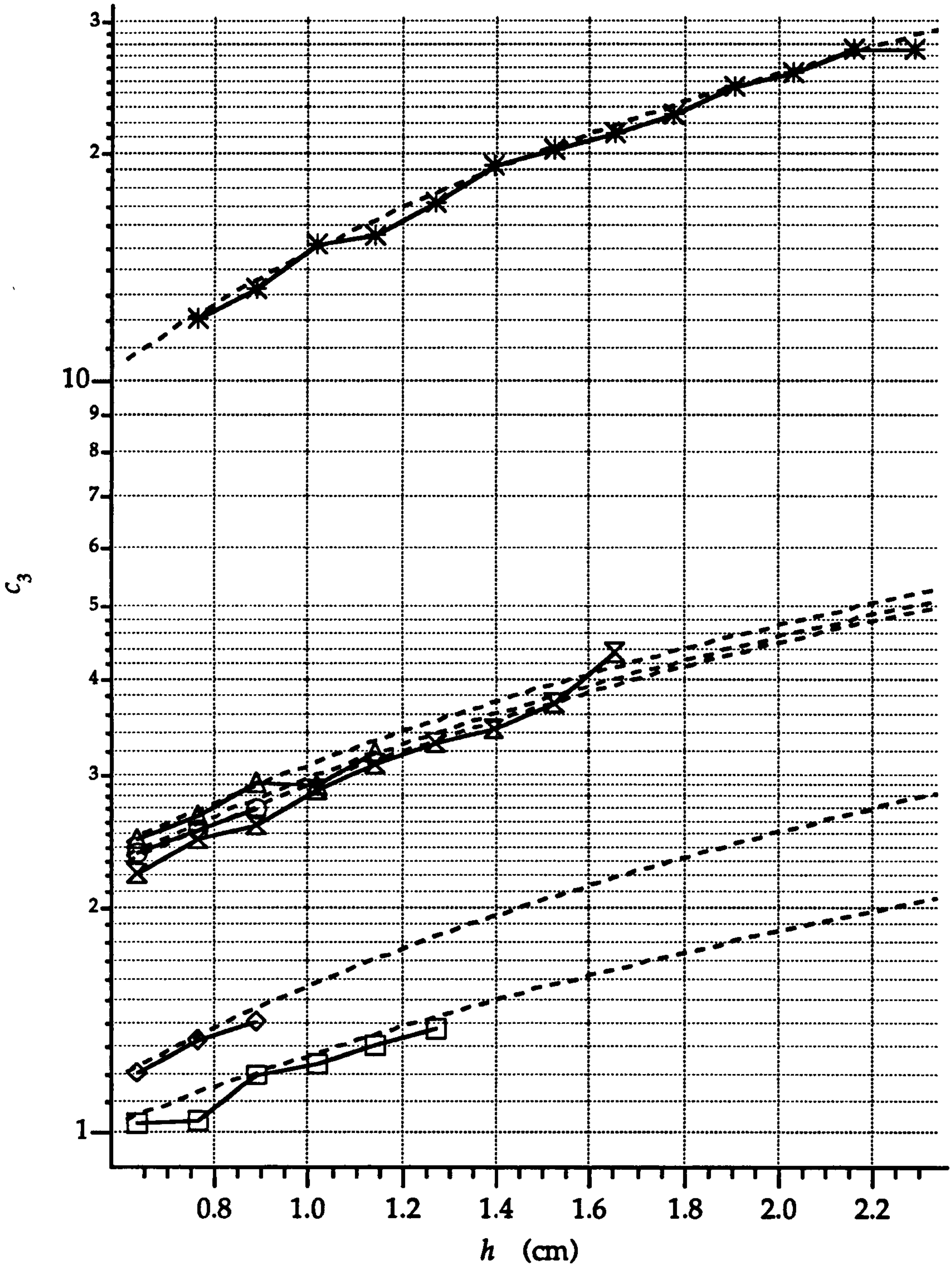

Figure 4.20. Parameters c_3 with approximate curves from Equation 4.14 for the 1.5 mm copper pin.

CHAPTER V

SUMMARY AND RECOMMENDATIONS

Summary

Studies have been conducted analyzing the voltage-current characteristics of an electrical plasma discharge in a static argon environment. Experimental voltage vs. current (V-I) curves were obtained for eight different electrode geometries at pressures from 745 to 3330 mmHg and arc gap spacing from .05 to 1.0 inch. All of the eight electrodes were cylindrical point geometries, but three were sharp steel pins with varying cone angles of 10°, 20°, and 30°, while the other five were copper pins with a fixed cone angle of 30° and varying tip radii of < 0.05 mm, 0.25 mm, 0.50 mm, 1.0 mm, and 1.5 mm.

Analyses first brought forward by Suits and others were used to develop relations describing the dependencies of characteristics such as threshold and breakdown voltages, critical field strength, arc diameter, and the general shape of the V-I curve, on the factors of pressure, gap spacing, and power input. Some of these relations describing the V-I characteristics were then verified with experimental data and their dependencies were quantified. Also obtained from the data were general trends that these characteristics followed with respect to the variations in electrode material and tip geometry.

In the Townsend region, it was found that the point of transition to corona or arc, as given by the threshold voltage, V_s, and threshold or onset current, i_s, became more stable and varied less with changes in pressure as the cone angle was increased. An increase in cone angle also corresponded to a decrease in the threshold current for fixed V_s. For the copper pins the curve traced out by the threshold voltage vs. i_s was virtually independent of the pressure, and similar to the steel pin case, an increase in tip radii corresponded to a decrease in onset current. So, in both cases, as the electrodes became more needle-like (decreasing tip radii or cone angle), the onset current increased for fixed values of the threshold voltage.

A similar behavior was noticed when the critical field strength was examined. As the electrode became more needle-like, the critical field strength, as given by the threshold voltage divided by the gap length, decreased. Both this effect and the one mentioned above about increasing onset current should be expected, since when an electrode becomes more needle-like, the electric field in close proximity to the tip is going to become stronger, requiring less applied voltage to maintain the same field strength. This means that the critical field strength for formation of the corona will be decreased for the same gap spacing, or that an electrode would reach its onset current at a lower value of the applied voltage, two aspects of the same phenomenon.

It was also found upon study of the critical field strength, that the assumption that V_s was a function only of the product of the gap spacing and the pressure, *hp*, held for the sharp pins, but for the pins with smaller curvature, lines of constant pressure began to appear in the plots, being more apparent for the lower pressures.

In Figure 4.8, plots of the breakdown voltage for transition to an arc, V_b, were seen to show a clear linear dependence on the product *hp* for all of the electrodes, but they also showed that V_b has a dependence on the pressure aside from this product. An approximate functional form for V_b was arrived at, Equation 4.5, showing both of these effects, and values for the empirical constants were obtained from curve fits of this form applied to the experimental data. One obvious trend apparent in the curves of Figure 4.8 is that the breakdown voltage decreases with increasing pressure for fixed values of the product hp.

Inside the coronal region of the discharge, the current through the gap was seen to depend on the voltage across the gap according the Equation 4.6. However, it was shown that the parameter c_2 does not correspond to the threshold voltage V_s, as was suggested in Chapter 3, but instead it was found to have a linear dependence on both h and p separately as well as on their product. A functional form for c_1 was also obtained, Equation 4.8, showing an exponential dependence on both the pressure and gap spacing.

Finally, it was shown that in the arc region of the discharge, the voltage across the gap is an exponential function of the gap current given by Equation 4.11. Curve fits to the experimental data revealed that the parameters c_3 and n were not independent, more specifically, that c_3 had a linear dependence on h whose slope and intercept could be approximated by third order polynomials in n. The parameter n itself did not reveal its dependence on pressure, but in general was seen to decrease with increasing pressure and to decrease with increasing cone angle and tip radii. The values of n observed, however, differed considerably from those expected based on the analysis in Chapter 3 leading to Equation 3.35.

Recommendations

Again, it must be stated that this work was intended as only a first step along a line of research that would lead to an operational T-Layer type of MHD generator, as evidenced by the relatively broad scope and exploratory nature of the project. There is much more that needs to be done before this can happen. The most obvious of these tasks is the extension of the study of these discharge characteristics to a dynamic, flowing argon environment, or to environments with electronegative gases. It must also be extended to include more of the work done on characterizing the arc size and its dependence on power input, in order to better quantify the requirements needed to produce a usable T-layer in a flowing gaseous environment.

It is hoped that this line of research will continue, so that these steps may be carried out, and that this paper may serve to support these further steps.

LIST OF REFERENCES

LIST OF REFERENCES

[1] Rosa, Richard J., *Magnetohydrodynamic Energy Conversion*, McGraw-Hill, Inc., New York, NY, 1968.

[2] Sokolov, Veniamin S., "MHD Generators Employing the T-Layer Effect: An Overview of Research Work in the Field," English translation of the Russian paper from *MHD: Theory, Power Generation, and Technology 2*, Institute for High Temperatures, Academy of Sciences, USSR, 1986.

[3] Gove, P. B., *Webster's Third New International Dictionary*, Merriam-Webster Inc., Springfield, MA, 1986.

[4] Cobine, James D., *Gaseous Conductors, Theory and Engineering Applications*, p. 143, Dover Publications, Inc., New York, NY, 1958.

[5] Cobine, James D., *Gaseous Conductors, Theory and Engineering Applications*, pp. 147-149, Dover Publications, Inc., New York, NY, 1958.

[6] Townsend, J. S. *Electricity in Gases*, Oxford University Press, New York, NY, 1914.

[7] Thomson, G. P. *Conduction of Electricity Through Gases*, Cambridge University Press, London, 1933.

[8] Bauder, Uwe H. and Paul W. Schreiber, "The Optimization of Wall-Stabilized Arcs," *Proceedings of the IEEE*, vol. 59, no. 4, pp. 633-638, April 1971.

[9] Mihalas, Dimitri and Barbara Mihalas, *Foundations of Radiation Hydrodynamics*, Oxford University Press, New York, NY, 1984.

[10] Chandrasekhar, S. *Radiative Transfer*, Dover Publications, Inc., New York, NY, 1960.

[11] Elenbaas, *Physica*, vol. 4, p. 413, 1937.

[12] Suits, C. G. and H. Poritsky, "Application of Heat Transfer Data to Arc Characteristics," *Physical Review*, vol. 55, pp. 1184-1191, June 15, 1939.

[13] Suits, C. G., "Convection Currents in Arcs in Air," *Physical Review*, vol. 55, pp. 198-201, January 15, 1939.

[14] Kreith, Frank, *Principles of Heat Transfer*, Intext Educational Publishers, New York, NY, 1973.

[15] Cambel, Ali B., *Plasma Physics and Magnetofluid-Mechanics*, McGraw-Hill Book Company, Inc., New York, NY, 1963.

[16] Cobine, James D., *Gaseous Conductors, Theory and Engineering Applications*, p. 341, Dover Publications, Inc., New York, NY, 1958.

VITA

Roderick Greg Wamsley was born on June 23, 1970 in Ronan, Montana. He was raised in and attended high school in Charlo, Montana, where he graduated Valedictorian in May of 1988. He then moved to Bozeman, Montana to pursue undergraduate studies at Montana State University. During his time there he met and married the former Jodee J. Chaffee, and in May of 1992 he received with Highest Honors the Bachelor of Science degree in Physics with a minor in Mathematics. In June of 1992, he and his wife moved to Tullahoma, Tennessee, so that he may begin a position as student and Graduate Research Assistant at The University of Tennessee Space Institute, where he pursued studies toward and completed requirements for the Master of Science degree in Physics.